



**HAL**  
open science

## Structure and metamorphism of a subducted seamount (Zagros suture, Southern Iran)

Guillaume Bonnet, Philippe Agard, Samuel Angiboust, Patrick Monie, Marc Fournier, Benoît Caron, J. Omrani

► **To cite this version:**

Guillaume Bonnet, Philippe Agard, Samuel Angiboust, Patrick Monie, Marc Fournier, et al.. Structure and metamorphism of a subducted seamount (Zagros suture, Southern Iran). *Geosphere*, 2019, 16 (1), pp.62-81. 10.1130/GES02134.1 . hal-02510743

**HAL Id: hal-02510743**

<https://hal.umontpellier.fr/hal-02510743v1>

Submitted on 18 Mar 2020

**HAL** is a multi-disciplinary open access archive for the deposit and dissemination of scientific research documents, whether they are published or not. The documents may come from teaching and research institutions in France or abroad, or from public or private research centers.

L'archive ouverte pluridisciplinaire **HAL**, est destinée au dépôt et à la diffusion de documents scientifiques de niveau recherche, publiés ou non, émanant des établissements d'enseignement et de recherche français ou étrangers, des laboratoires publics ou privés.



Distributed under a Creative Commons Attribution - NonCommercial 4.0 International License

GEOSPHERE, v. 16, no. 1

<https://doi.org/10.1130/GES02134.1>

12 figures; 2 tables; 1 supplemental file

CORRESPONDENCE: [gbonnet01@gmail.com](mailto:gbonnet01@gmail.com)

CITATION: Bonnet, G., Agard, P., Angiboust, S., Monié, P., Fournier, M., Caron, B., and Omrani, J., 2020, Structure and metamorphism of a subducted seamount (Zagros suture, Southern Iran). *Geosphere*, v. 16, no. 1, p. 62–81, <https://doi.org/10.1130/GES02134.1>.

Science Editor: Shanaka de Silva  
Guest Associate Editor: Gray E. Bebout

Received 25 February 2019  
Revision received 3 July 2019  
Accepted 14 October 2019

Published online 21 November 2019



This paper is published under the terms of the CC-BY-NC license.

© 2019 The Authors

# Structure and metamorphism of a subducted seamount (Zagros suture, Southern Iran)

G. Bonnet<sup>1,2</sup>, P. Agard<sup>1</sup>, S. Angiboust<sup>3</sup>, P. Monié<sup>4</sup>, M. Fournier<sup>1</sup>, B. Caron<sup>1</sup>, and J. Omrani<sup>5</sup>

<sup>1</sup>Sorbonne Université, CNRS-INSU, Institut des Sciences de la Terre de Paris, ISTE P UMR 7193, CNRS F-75005 Paris, France

<sup>2</sup>Earth Research Institute, University of California, Santa Barbara, California 93106, USA

<sup>3</sup>Université de Paris, Institut de Physique du Globe de Paris, CNRS, F-75005 Paris, France

<sup>4</sup>Géosciences Montpellier UMR-CNRS 5243, Place E. Bataillon, 34090 Montpellier, France

<sup>5</sup>Geological Survey of Iran, Tehran, Iran

## ABSTRACT

**Millions of seamounts on modern and past seafloor end up being subducted, and only small pieces are recovered in suture zones. How they are metamorphosed and deformed is, however, critical to understand how seamount subduction can impact subduction zone geometry, fluid circulation or seismogenic conditions, and more generally to trace physical conditions along the subduction boundary. Since geophysical studies mostly reach the shallowest subducted seamounts and miss internal structures due to low resolution, there is a high need for fossil seamount exposures. We herein report on a fully exposed, 3D example of seamount that we discovered in the Siah Kuh massif, Southern Iran. Through a series of sections across the whole massif and the combination of magmatic-metamorphic-sedimentary petrological data, we document several distinct stages associated with seamount build-up on the seafloor and with subduction. In particular, we constrain different stages of metamorphism and associated mineralogy, with precise conditions for subduction-related metamorphism around 250 °C and 0.7 GPa, in the middle of the seismogenic zone. Extensive examination of the seismogenic potential of the Siah Kuh seamount reveals that it was not a large earthquake asperity (despite the report of a rare example of cm-scale, high-pressure pseudotachylyte in this study), and that it possibly behaved as a barrier to earthquake propagation. Finally, we discuss the nature of high-pressure fluid circulation preserved in this seamount.**

## 1. INTRODUCTION

Seamounts are “geographically isolated topographic feature[s] on the seafloor taller than 100 m, including ones whose summit regions may temporarily emerge above sea level, but not including features that are located on continental shelves or that are part of other major landmasses” (Staudigel et al., 2010). Although most seamounts were recognized in the early stages of plate tectonics as products of mantle upwelling at hotspots (Wilson, 1965; Morgan, 1971), many of them also form by hydration-driven melting of the forearc mantle of subduction zones (e.g., Reagan et al., 2010) or close to ocean ridges (e.g., East Pacific Rise seamounts, Niu et al., 1999). There are more than 100,000 seamounts on present-day seafloor (Hillier and Watts, 2007; Wessel et al., 2010); most of these seamounts will at some point enter subduction zones (e.g., Lallemand et al., 1989; Ranero and von Huene, 2000). Therefore, understanding how they form and evolve is critical to assess natural hazards such as subduction earthquakes, volcanic activity, or slope instabilities that may result in tsunamis (Lipman et al., 1988; Keating and McGuire, 2000).

The link between the subduction of rough seafloor and subduction earthquakes has been a matter of considerable debate since it was recognized that seamount size scales with the largest earthquake asperities (Cloos, 1992). However, the observation that zones where rough seafloor enters subduction may coincide with seismic gaps (i.e., zones with no record of earthquakes, Kelleher and McCann, 1976; Lallemand et al., 2018; van Rijsingen et al., 2018) suggests that (1) seamounts are probably not seismic asperities, and (2) they might also act as barriers that

block rupture propagation and limit the magnitude of megathrust earthquakes (Geersen et al., 2015). While several studies tend to confirm this (e.g., Wang and Bilek, 2011, 2014), direct evidence is still missing.

Seamounts are also suspected to impact upper-plate topography and trigger subduction erosion (i.e., removal of material from the upper plate; Vannucchi et al., 2006; Clarke et al., 2018) and to experience partial decapitation (Cloos, 1993; Cloos and Shreve, 1996; shallow, small-volume [Mariana-type margins] and deeper, larger volume, i.e., at the base of the accretionary wedge [Chile-type margins]). The small volumes of subducted seamounts recovered in underplated units suggest that most of them get subducted down to the deep mantle, like “normal” oceanic crust. In all cases, they are suspected to have a large impact on the long-term coupling of the subduction interface (Agard et al., 2018).

While oceanographic studies inform us about present-day seamounts, geophysical imaging of subducting seamounts meets several issues. Resolution, for example, is generally too low to distinguish deformation features within seamounts (with the notable exception of the study of Park et al., 1999). Additionally, geophysical studies access only the top 10–15 km, and imaging the nature of the subducting plate below this is limited to very exceptional setups (e.g., Singh et al., 2011).

Exposed examples of fossil seamounts are therefore paramount to directly access a several million-year-long history on ocean floor and in a subduction zone, as well as internal deformation and metamorphism. As earlier mentioned, preserved fossil examples of seamounts are rare. Some escaped subduction and may be good places to study oceanic

processes (e.g., Slave Province, Corcoran, 2000; Nicasio Reservoir Terrane, Schnur and Gilbert, 2012). Yet only two fossil seamounts have so far been reported as having once been subducted: the Snow Mountain Volcanic Complex in the Franciscan complex (MacPherson, 1983; Shervais et al., 2005) and the Anarak-Kabudan seamounts in Central Iran (Bagheri and Stampfli, 2008). The Snow Mountain Volcanic Complex is a  $20 \times 15$ -km-large, at least 1-km-thick oceanic unit that was incipiently metamorphosed at blueschist facies, as shown by the occurrence of metamorphic lawsonite and aragonite (MacPherson, 1983). The Anarak unit is a  $\sim 30 \times 15$ -km-large and  $\leq 500$ -m-thick unit interpreted to be a seamount. It is composed of bimodal volcanics (alkali basalts and rhyolite) overlain by a carbonate atoll and a pelagic veneer; however, the current structure has been strongly dismembered during Paleotethys closure and late faulting. It is affected by high-pressure–low-temperature metamorphism, with a continuous evolution from pumpellyite-actinolite facies to albite-lawsonite and epidote-crossite facies. The Kabudan Guyot has a smaller size ( $\sim 20 \times 20$  km large), and only the carbonate cap, pelagic veneer, and slope facies deposits are exposed. Bagheri and Stampfli (2008) argue that surrounding tectonic structures derive in part from upper-plate deformation due to seamount subduction.

While volcanism was studied in detail in the Snow Mountain Volcanic Complex and the sedimentary evolution in the Anarak-Kabudan seamounts, little has been done so far to characterize the volcanism, sedimentation, subduction-related deformation, incipient metamorphism and fluid circulation in a single seamount. These observations require a fully exposed, almost intact, 3D fossil subducted seamount, as is the Siah Kuh seamount reported here.

## 2. GEOLOGICAL SETTING

The Zagros Mountains in southern Iran result from long-lived convergence that is still active today between the Arabian and the Eurasian plates (convergence rates of  $22 \pm 2$  mm/yr; Vernant et al., 2004; Masson et al., 2007). Ophiolite belts, locally referred to as the Colored M $\acute{e}$ lange (Gansser, 1955),

are the remnants of the Neotethys ocean separating Arabia from Eurasia (Fig. 1A). Subduction of the Neotethys under Eurasia is testified to by Jurassic to Quaternary magmatism in the Sanandaj-Sirjan zone (SSZ) and in the Urumieh Dokhtar magmatic arc (UDMA; mentioned as “arc magmatism” on Fig. 1A). While collisional structures are well characterized in the Zagros fold-and-thrust belt and in the lower part of the Crush Zone (Agard et al., 2005; Molinaro et al., 2005a; Omrani et al., 2008), oceanic material is little affected by collision-related deformation and metamorphism (Agard et al., 2006). Slab break-off occurred during the Pliocene and is characterized by adakitic magmatism in the UDMA (Omrani et al., 2008) and regional uplift in the Central Iranian Plateau (Molinaro et al., 2005b).

Despite this long subduction history, only a handful of exposures of blueschist-facies rocks are recovered from this subduction: the Hajiabad-Esfandagheh zone in southeastern Zagros, close to the Makran, is the only place where high-pressure–low-temperature metamorphism has been recorded in the Zagros range (Agard et al., 2006; synthetic map in Fig. 1B).

In particular, the Soghan region in the northeastern part of the Hajiabad-Esfandagheh zone (Fig. 1B), has been recognized as a stack of high-pressure nappes by Agard et al. (2006): the uppermost Ashin unit, the intermediate Seghin unit, and the lowermost “Colored M $\acute{e}$ lange” zone, here named the Siah Kuh unit. The Ashin unit is made of a complex imbrication of upper blueschist to epidote-amphibolite facies metasedimentary and metavolcanics overlying a thick dunite massif. The Seghin unit is in turn composed of hectometer-sized slices of blueschist-facies metabasites in a serpentinite matrix. The Siah Kuh unit has no characteristics of a m $\acute{e}$ lange and is an almost continuous piece of oceanic lithosphere with serpentinite, gabbro, basalt, and associated hyaloclastite, pelagic, and platform sediments (Sabzehei, 1974), and it is likely a seamount (Angiboust et al., 2016; Bonnet et al., 2019). The report of boninitic lavas (Moghadam et al., 2013) suggests formation of Siah Kuh above an intra-oceanic subduction zone. Traces of incipient metamorphism have been recognized in the Siah Kuh unit, in particular with the occurrence

of lawsonite and aragonite (Sabzehei, 1974; Angiboust et al., 2016). Sabzehei (1974) also mentions the occurrence of glaucophane and aegirine, but these might belong to the overlying Seghin unit. Pressure-temperature (P-T) conditions reach 1.1–1.3 GPa and 520–580 °C for the Ashin unit and 1.7 GPa and 500 °C for the Seghin blueschists (Agard et al., 2006). The occurrence of high-pressure minerals in the Siah Kuh unit hints to incipient blueschist-facies conditions (Sabzehei, 1974; Angiboust et al., 2016; Bonnet et al., 2019). Several geochronology studies have tried to date the high-pressure metamorphism of the Zagros blueschists: K-Ar dating of white mica in the Ashin unit yields ages of ca. 100 Ma (Delaloye and Desmons, 1980), in situ Ar-Ar dates of phengite are 110–82 Ma in the Ashin unit and 127–95 Ma for the Seghin unit (Agard et al., 2006), while step-heating Ar-Ar dates of phengites are 105–93 Ma for the Ashin unit and 85–80 Ma for the Seghin unit (Moni $\acute{e}$  and Agard, 2009). Rb-Sr ages are more scattered, between 135 and 79 Ma for the Ashin unit and 95–62 Ma for the Seghin unit (Angiboust et al., 2016; Moghadam et al., 2017).

The objectives of this study are to precisely map and characterize the internal structure of the Siah Kuh unit, to demonstrate that it once was a seamount on the ocean floor and was later subducted, and to characterize oceanic and subduction structures, metamorphism, and the nature of fluid circulating at depth.

## 3. STRUCTURES

The Siah Kuh unit lies structurally below the Seghin unit and is separated from it by a sediment-dominated sliver made of radiolarian cherts and fine basaltic tuffs mixed with pillow basalt and gabbro. Structures are summed up on the map of Figure 1C and cross sections of Figure 2.

### 3.1 Ocean-Derived Structures

The Siah Kuh massif is composed of two main units. The heart of Siah Kuh, herein mentioned as A<sub>1</sub> unit, is composed, from bottom to top, of a

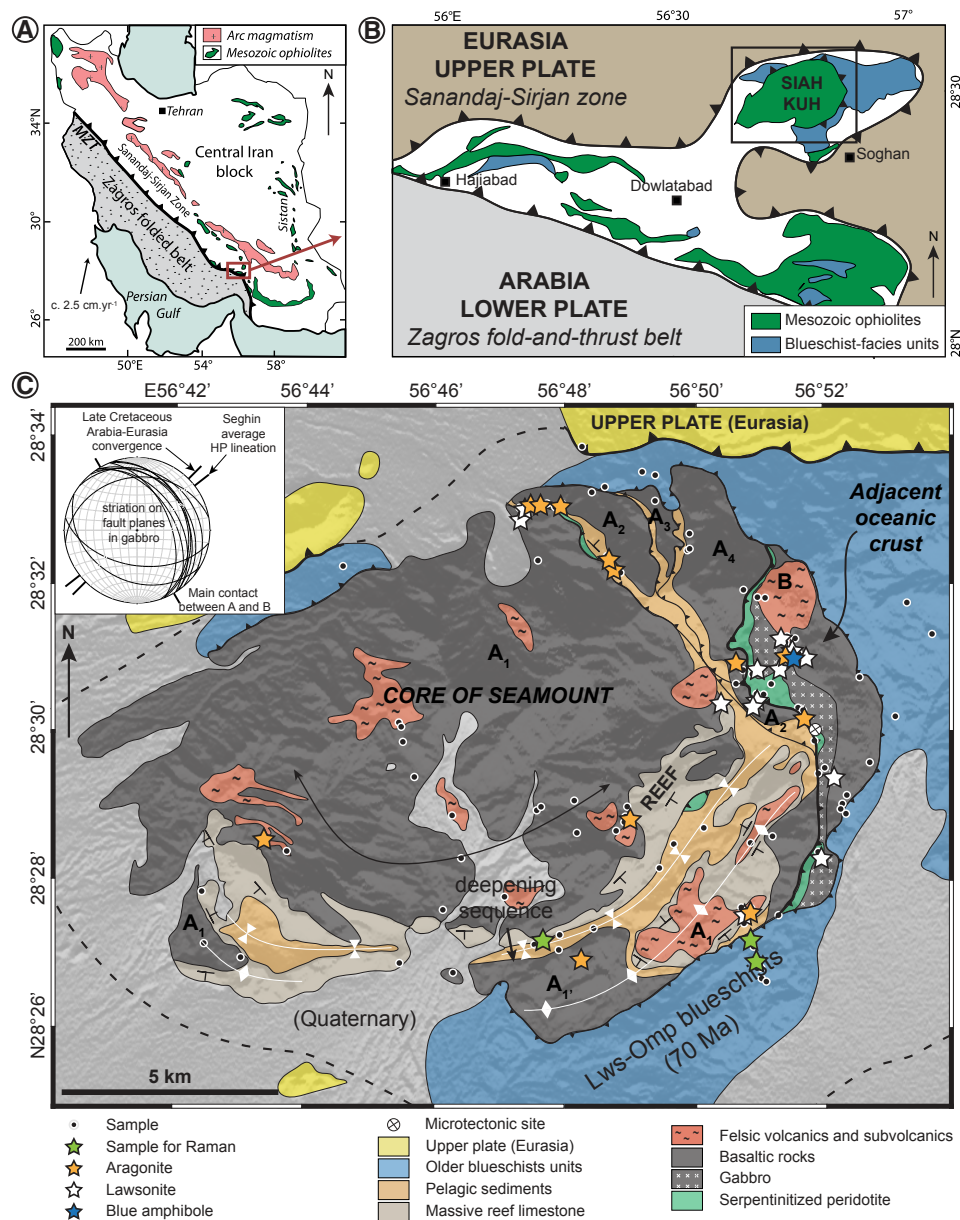


**Figure 1.** Geological context and structural framework of the Siah Kuh unit. (A) Map of Iran highlighting Mesozoic arc and volcanic arc in the Zagros orogen, after Angiboust et al. (2016); (B) zoom on the Hajiabad-Esfandagheh zone, modified after Angiboust et al. (2016); and (C) map of the Siah Kuh seamount after Bonnet et al. (2019); inset: polar projection of fault orientation and striation. Lws-Omp—lawsonite-omphacite, MZT—Main Zagros Thrust.

>1-km-thick pile of pillow basalts (Fig. 3A), hyaloclastite, pillow breccia and basaltic flows (Fig. 3B). These volcanic rocks are intruded by felsic sub-volcanics (hereafter plutons; e.g., Fig. 3C), with local contact metamorphism; these plutons are linked with rhyodacitic lavas. All these structures are conformably overlain by a massive (up to 50-m-thick, but variably thick) gray limestone bed (Figs. 3C–E), typical of relatively shallow platform depositional environments, visible only in the southern and eastern parts of Siah Kuh (likely of Upper Campanian to Maastrichtian age; Sabzehei, 1974). This gray limestone includes in places chert nodules and/or regularly spaced chert layers. Some exposures are composed of a consolidated rudstone to carbonate conglomerate comprising cm-sized clasts of the gray limestone in a darker carbonate matrix; these exposures testify to a high-energy, possibly wave-controlled sedimentary reworking (Fig. 3F). This limestone is unevenly recrystallized, and fossils (preserved in places) indicate a shallow-water ecosystem: gastropods (Fig. 3G), foraminifera (Fig. 3H), urchin spines, and bivalve shells. The gray limestone bed is overlain by a 200- to 500-m-thick deepening sedimentary sequence (which directly overlies basalt and hyaloclastite in the northern part of Siah Kuh), composed of tuffaceous sandstone, finely stratified pink pelagic limestone, and red radiolarian chert (Figs. 3E and 3M). Exposures on the northern side of Siah Kuh represent deeper environments as demonstrated by the fact that pelagic sediments directly rest on top of the lavas of A<sub>1</sub>, with no reef limestone intercalation. Debris flows within this sequence are characterized by variably sized lenses (olistoliths) of massive or pelagic limestone, radiolarian chert, and basalt in a tuffaceous or limestone matrix (Figs. 3I–3K), as well as slumps of turbiditic material, either consolidated or not, some of which appear locally as sheath folds (Fig. 3L). Some decameter-sized pods of serpentinite (e.g., Fig. 4F) are found within the tuffaceous sandstone all around Siah Kuh, but they never make a continuous layer. Parts of this sedimentary sequence are locally intruded by the felsic plutons of the core of Siah Kuh.

The sedimentary sequence is conformably overlain by another set of pillow basalts, hyaloclastites, and basaltic flows; this set testifies to the resumption of volcanic activity and a rejuvenation of the magmatic

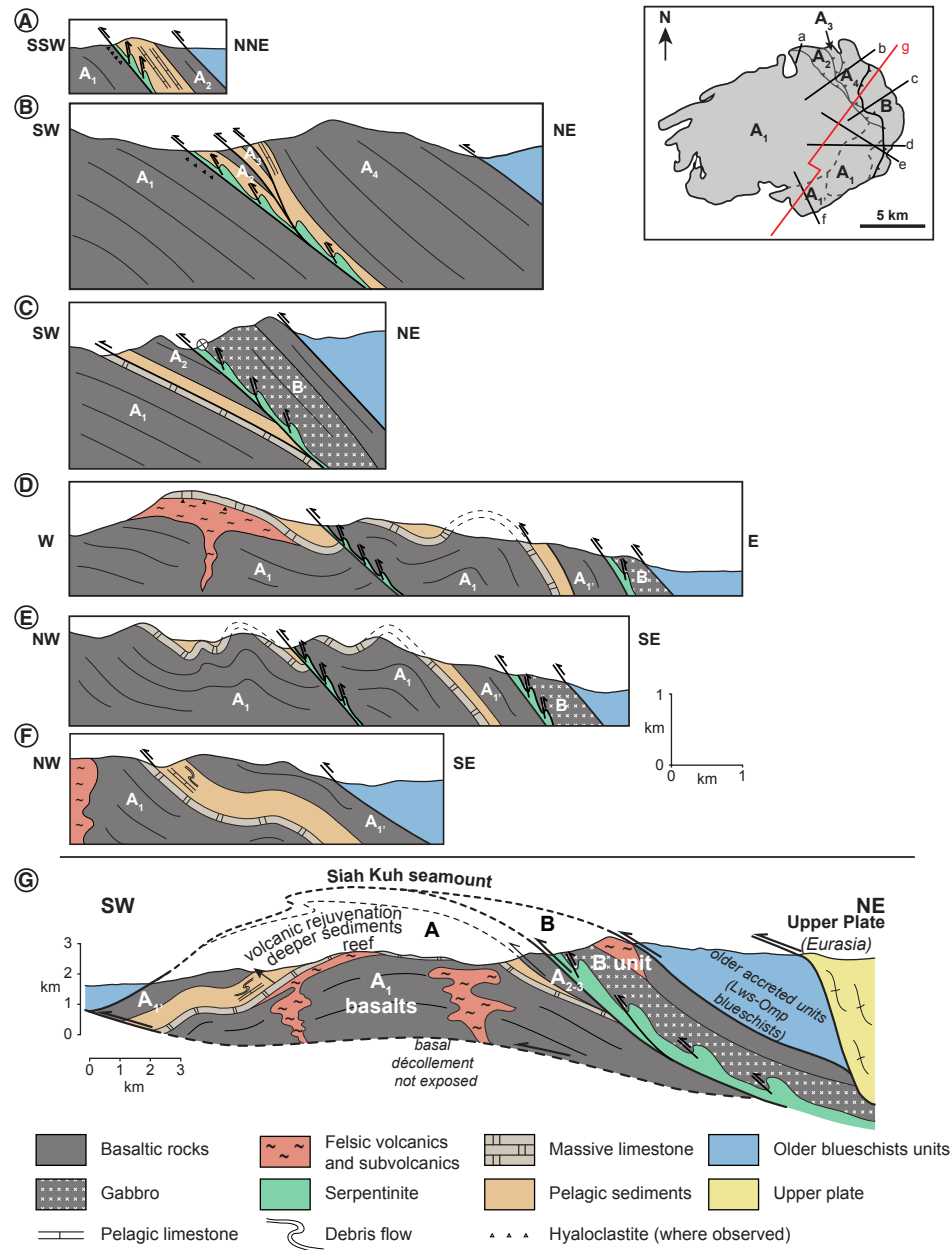


Figure 2. Cross sections through the Siah Kuh seamount. Synthetic cross section after Bonnet et al. (2019). Lws-Omp—lawsonite-omphacite.

edifice (namely, the A<sub>1</sub>, A<sub>2</sub>, A<sub>3</sub>, and A<sub>4</sub> units, Figs. 3C, 3E, 3M, and 3N), yet with no felsic magmatism. Continuous layers of pelagic sediments are intercalated with the basalts of this rejuvenation event (Fig. 3N). This rejuvenation event is geographically discontinuous and consists of five 1- to 3-km-wide massifs.

The A unit has all the characteristics of a seamount (i.e., size, magmatic activity, and reef limestone), which may have reached (and in any case may have been close to) sea level at the end of the first phase of activity, but eventually subsided to greater, possibly abyssal depths.

In the northeastern part of Siah Kuh, the rejuvenation events are tectonically overthrust by the B unit, which consists, from bottom to top, of a fully serpentinized ultramafic base (maximum 800 m thick, but thinning and disappearing to the north and east of Siah Kuh) enclosing meter-sized gabbro pods, an almost continuous gabbro layer intruding serpentinite, and, finally, rhyodacitic lava and basalt with minor sediments (Fig. 3O). It is proposed that this B unit is a lateral equivalent of the A unit on the side of the seamount.

### 3.2 Subduction-Derived Structures

The Siah Kuh unit was subsequently subducted, and subduction-related deformation affected the whole edifice. The deformation is clearly visible in sheared pillow breccia in the north part of Siah Kuh; these pillow breccia record a top to the SW sense of shear (Fig. 4A). Deformation is conspicuous in the sedimentary cover of the A<sub>1</sub> unit, where the massive limestone is highly and sometimes tightly folded (Figs. 3, 4B, and 4C), but is less obvious in basalts due to the absence of layering. However, portions of the A<sub>1</sub> unit are folded and form large-scale anticlines, and even thrust on the core of A<sub>1</sub> unit (cross sections of Figs. 2 and 4C). The contact between A<sub>1</sub> and the lavas of the magmatic rejuvenation event is locally not faulted in the southeast part of Siah Kuh (contact between A<sub>1</sub> and A<sub>1</sub>, Fig. 3C). In general, the base of the detrital-pelagic sequence acts as a décollement with hectometer-scale displacement and strongly sheared (top to the W) serpentinite pods pinched inside the fault (Figs. 4E and 4F).

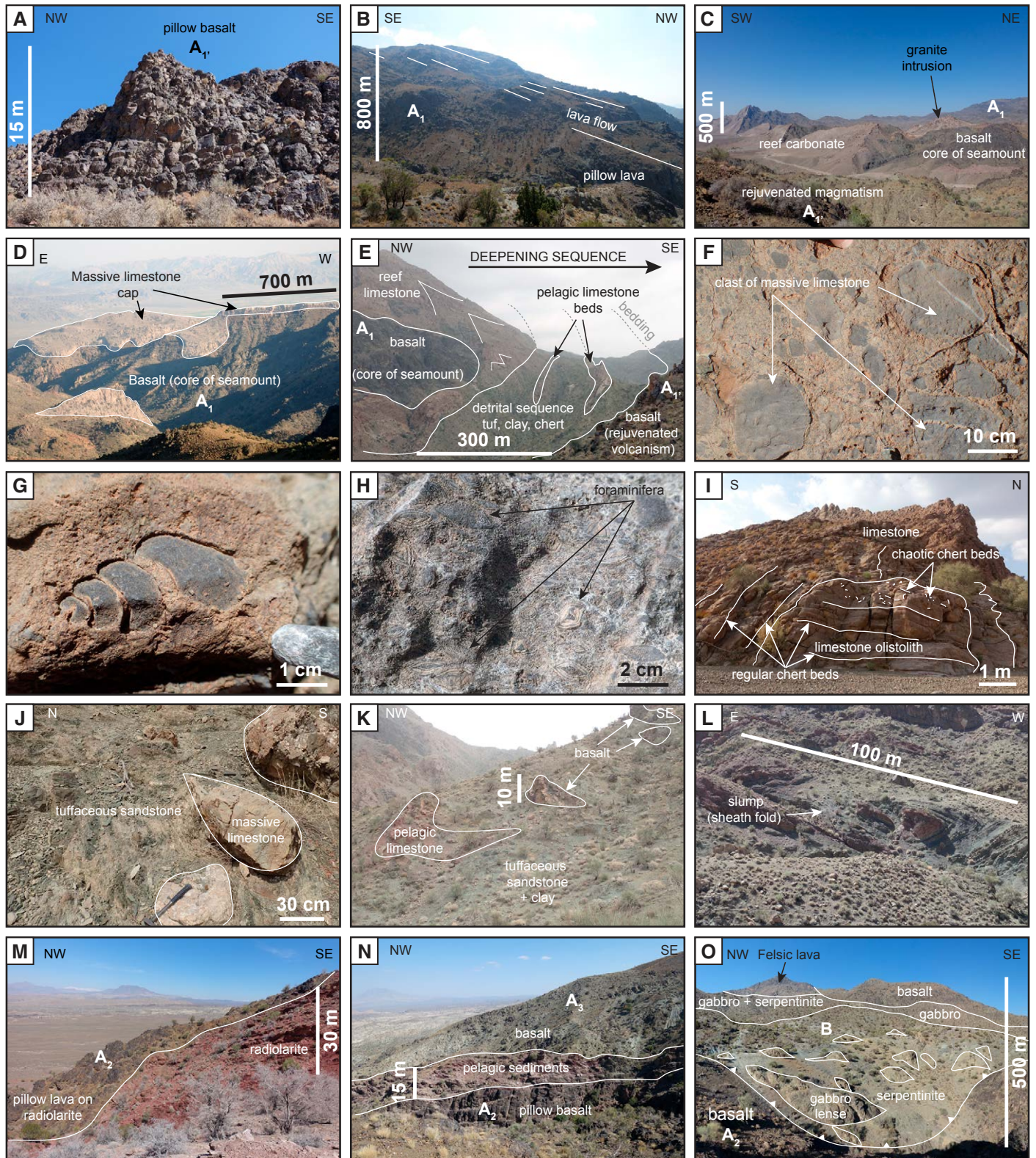


**Figure 3. Pictures of pre-subduction structures. (A)** Pillow basalt cliff in the  $A_1$  unit; **(B)** basalt flow on top of pillow basalts in the  $A_1$  unit; **(C)** massive limestone overlying basalt from the core of the seamount, a granite pluton intrudes the basalts in the core of the seamount and rejuvenated magmatism of the  $A_1$  unit is visible in the bottom part of the picture; **(D)** carbonate breccia, high-energy reworking of a carbonate platform; **(E)** gastropod in carbonate; **(F)** foraminifera beds in the massive limestone; **(G)** sedimentary sequence on top of the  $A_1$  unit: massive "reef" limestone overlies basalts from the core of the seamount, with a deepening detrital sequence on top of the massive limestone,  $A_1$  (rejuvenated) unit on the right; **(H)** small blocks of limestone in a debris flow with a tuffaceous sandstone matrix; **(I)** large blocks of limestone and basalt in a debris flow with a tuffaceous sandstone and clay matrix; **(J)** limestone olistolith within the massive limestone cliff; **(K)** sheath fold in pelagic sediments resulting from slumping; **(L)** resumption of basaltic volcanism after deep sedimentation in the  $A_2$  unit; **(M)** continuous layer of pelagic sediments (pelagic limestone and radiolarian chert) within the basalts of the  $A_2$  unit; **(N)** structure of the B unit; and **(O)** structure of the B unit showing an ultramafic base, felsic lavas, a gabbroic intrusion, and basalts erupted on top of the sequence.

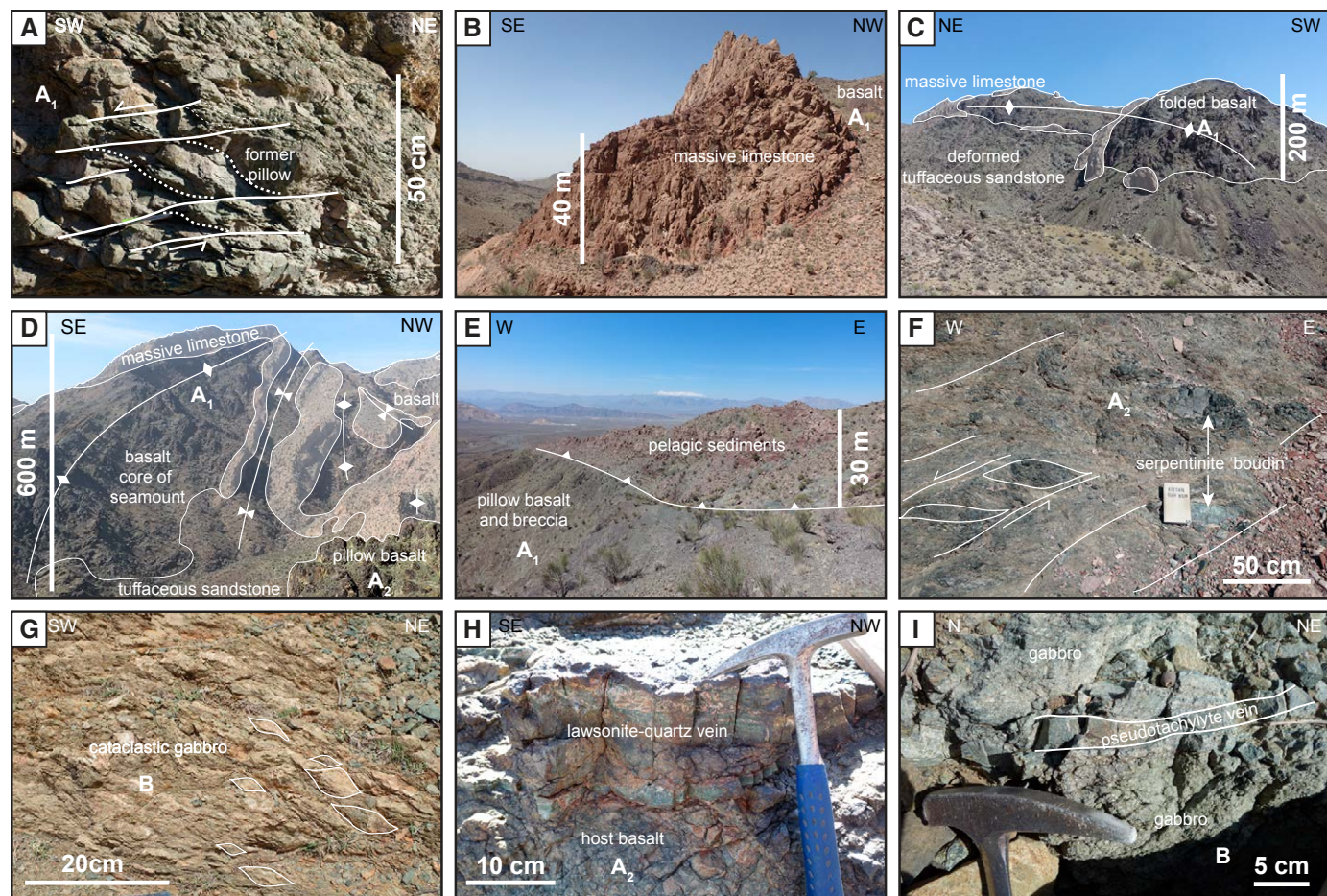


**Figure 4.** Pictures of subduction-related structures. (A) Sheared pillows and pillow breccia in the A unit; (B) folded massive limestone on top of the A unit; (C) large-scale anticline in the A unit affecting basalt and massive limestone; (D) tight folding of limestone of the core of the seamount; (E) thrusting (décollement) of pelagic sediments on top of the A unit; (F) sheared serpentinite pod pinched in a fault zone; (G) cataclastically deformed gabbro at the base of the B unit; (H) lawsonite-quartz vein with basalt clasts in a basalt of the A<sub>2</sub> unit; and (I) pseudotachylyte vein in gabbro of the B unit.

The main fault within Siah Kuh is the thrust fault separating the A unit from the B unit (mainly observed in the northeastern part of Siah Kuh) and is associated with kilometer-scale displacement, since it is rooting in the mantle (i.e., the serpentinite base of unit B). Some gabbro exposures at the base of the B unit are cataclastically deformed, with many cm<sup>2</sup>-scale slip planes along grain boundaries

(Fig. 4G). This deformation is accommodated over an ~100-m-thick zone. Striations and rare stretching lineations in the gabbro indicate a dominant displacement along N060° (inset in Fig. 1C), with a sense of shear dominantly top to the NE (Fig. 4G). A network of lawsonite-quartz veins is observed along this fault, within basalt (Fig. 4H); these veins are high-pressure brittle events, likely due to hydraulic brecciation.

Lawsonite veins are frequent in the basalts of the top of the A unit. Gabbros of the B unit are in most cases isotropic, but they are crossed by small (< mm-thick) shear bands filled by chlorite or amphibole. One example of a pseudotachylyte vein in gabbro was found within Siah Kuh (Bonnet et al., 2019; Fig. 4I); this vein is associated with centimeter-to-decimeter displacement.

## ■ 4. PETROGRAPHY, GEOCHEMISTRY, AND P-T ESTIMATES

### 4.1 Analytical Methods

A selection of samples is given in Table 1. Analyses and imaging of thin sections were done at the scanning electron microscopy (SEM) facilities at École Normale Supérieure (ENS), Institut de Physique du Globe (IPGP), and Institut des Sciences de la Terre de Paris (ISTeP); and other analyses have been done using the electron microprobe SX5 and SX100 (15 kV, 10 nA, 1  $\mu\text{m}$  spot and wavelength-dispersive spectrometry [WDS]) at the CAMPARIS facility (Sorbonne Université), with diopside (Si, Ca, and Mg), orthoclase (K and Al),  $\text{MnTiO}_3$  (Mn and Ti),  $\text{Fe}_2\text{O}_3$  (Fe), and albite (Na) as standards. Structural formulas were calculated with  $\text{Fe}^{3+}$  estimated using the method of Leake et al. (1997) for amphibole, and considering all iron as ferric in lawsonite. Analyses of pseudotachylyte minerals were exclusively performed by energy-dispersive spectroscopy (EDS) quantification at the SEM due to small crystal size; however, the precision of the analyses was confirmed by structural formula calculations.

Element maps were captured with the electron microprobe using similar beam conditions as for points, with a dwell time of 140 ms and step size of 3  $\mu\text{m}$  for lawsonite and 100 ms/0.2  $\mu\text{m}$  for amphibole, and they were processed using XMapTools v. 2.5.1 (Lanari et al., 2014).

In situ trace-element content of silicates (lawsonite, pumpellyite, and amphibole, analyzed in polished 100  $\mu\text{m}$  section 1529) was determined by laser ablation–inductively coupled plasma mass spectrometry (LA-ICP-MS) (Photon Machine Analyst G2 193 nm ArF excimer laser ablation system coupled to an Agilent 8880 QQQ-ICP-MS) at the ALIPP6 laboratory, ISTeP, Sorbonne Université. The background was measured for 18 s before and after sample analysis by laser ablation. Samples were spot ablated for 60 s at an 8 Hz repetition rate in a helium gas atmosphere using a 40  $\mu\text{m}$  beam and laser energy of 3.54 J/cm<sup>2</sup>. Argon was employed as the plasma gas. International glass standard BHVO2G (Jochum et al., 2005) was used as the primary standard to calculate elemental concentrations

(using <sup>27</sup>Al as the internal standard element with electron probe microanalyzer [EPMA] analyses of minerals) and to correct for instrument drift. The mass spectra were reduced using an in-house Excel spreadsheet and macro. Repeated analyses of international standards ATHO-G and BCR2-G were used to estimate the precision of the analyses. Analyses reproducibility is within 1%–15% for most trace elements, except Cs (62%) and Be (36%).

Raman spectroscopy on carbonaceous matter (RSCM) has been performed using Raman spectrometer Renishaw InVia at ENS on three samples. Peak deconvolution was done using PeakFit<sup>®</sup>. Raman spectroscopy was also used to determine the nature of polymorphs of calcium carbonates and serpentine (Gropo et al., 2006; Schwartz et al., 2013; De La Pierre et al., 2014).

Mineral abbreviations are after Whitney and Evans (2010).

### 4.2 Textures

The whole Siah Kuh unit is strongly affected by hydrothermal recrystallization close to the seafloor. Destabilization of magmatic minerals is ubiquitous: glassy mesostase is recrystallized, and magmatic pyroxene and feldspars are partly replaced by albite, prehnite, pumpellyite, epidote, and chlorite, sometimes as veins (Figs. 5A and 5B). This destabilization characterizes the hydration of magmatic rocks by hydrothermal processes at the seafloor.

High-temperature contact metamorphism is located near felsic plutons. It affects mostly the sediments within the A unit. Birefringent garnet (hydrogarnet) growth followed by optically isotropic (nominally anhydrous) garnet growth is visible in calc-silicate sediments from the heart of Siah Kuh (Fig. 5C), and red contact areolas are visible from afar in the massive limestone bed.

High-pressure recrystallization imprinting within Siah Kuh is localized and mostly occurs in the northeastern part of Siah Kuh. Lawsonite occurs in veins or as plagioclase pseudomorphs (Figs 5D–5I). Lawsonite-quartz veins brecciate greenschist-facies hydrothermalized basalt, which contains pumpellyite veins from a previous event (Figs. 5D and 5E).

However, growth of pumpellyite around lawsonite also shows that some of the pumpellyite is retrograde (Fig. 5F). Lawsonite crystals are euhedral, some have greenish cores and colorless rims, with pumpellyite retrogression rims. Rhyolites within the core of Siah Kuh also contain lawsonite within veins (Fig. 5H). Gabbros are affected by (partly high-pressure) recrystallization: plagioclase is pseudomorphed into lawsonite and pumpellyite, while pyroxene, former olivine, and/or hydrothermal and/or greenschist-facies amphiboles have overgrowths of green amphibole (Figs. 5I–5L).

Aragonite veins are found within basalt, rhyolite, and carbonates (Fig. 5M). One sample of tuffaceous sandstone contains albite and disorganized mica and amphibole and is crosscut by epidote-titanite veins (Fig. 5N). Serpentinite is mostly made of lizardite, with bastite and mesh textures.

The single pseudotachylyte vein in Siah Kuh contains fine magmatic crystals of twinned plagioclase (forming chromosomes) locally surrounded by clinopyroxene (Figs. 6A and 6B). Sulfide minerals are abundant in the pseudotachylyte. Some of the plagioclase-clinopyroxene crystals are arranged as spherulite (Fig. 6B). A former magmatic glass is replaced by fine (a few micrometers long) crystals of green amphibole and albite. These features correspond to the altered pseudotachylyte identification criteria described by Kirkpatrick and Rowe (2013). One glaucophane crystal was found within the tremolite-albite matrix (Fig. 6C).

The southern limit of the Siah Kuh seamount is separated from the Seghin unit by a 300–500-m-thick sliver of metasediments (tuffs and radiolarian cherts) associated with a few microgabbro and metabasalt blocks. Metamorphism of this unit has not been further studied here; however, one sample was collected for temperature determination.

### 4.3 Mineral Compositions

Metamorphic minerals have been analyzed in eight samples: metagabbro (1530, 1531, 1532, 1727, and 1728), lawsonite-quartz vein (and metabasalts matrix, 1734 and 1529), and metasediment (1722). Representative analyses are shown in Table 2.

TABLE 1. SAMPLE DESCRIPTION, LOCATION, MINERALOGY, AND TECHNIQUES USED

Sample	Description	Unit	Latitude N	Longitude E	Lws	Arg	Blue amp.	SEM/EDS	EPMA	Raman	Ar-Ar
1428	Fracture in basalt	Intermediate sliver	28°28.825'	56°52.260'			x				
1513	Organic-matter-rich carbonate	Seghin	28°26.780'	56°50.943'						x	
1517	Tuffaceous sandstone	Intermediate sliver	28°27.368'	56°50.723'						x	
1518	Rhyolite	A1	28°27.462'	56°50.738'	x	x		x			
1529	Lawsonite vein in basalt	B	28°30.887'	56°51.725'	x			x	x		
1530	Pseudotachylyte and host gabbro	B	28°30.935'	56°51.572'	x		x	x	x		
1531	Gabbro	B	28°30.963'	56°51.525'	x			x	x		
1532	Gabbro	B	28°31.082'	56°51.397'	x						
1603	Calc-silicate metasediment	A1	28°29.745'	56°45.539'							
1607	Basalt	A1	28°32.719'	56°47.345'	x						
1609	Basalt	A2	28°32.945'	56°47.754'		x					
1610	Basalt	A2	28°32.099'	56°48.698'		x					
1613	Pillow basalt	A4	28°32.987'	56°49.403'							
1625	Lawsonite vein in andesite	B	28°30.870'	56°51.719'	x						
1628	Aragonite vein in basalt	A1	28°28.433'	56°43.412'		x					
1632	Tuffaceous sandstone	A1	28°27.178'	56°47.708'						x	
1634	Basalt	A1'	28°26.821'	56°48.278'		x					
1637	Pillow breccia	B	28°30.045'	56°51.600'		x					
1640	Lawsonite vein in basalt	A2	28°30.321'	56°50.949'	x						
1702	Tuff	A2	28°32.924'	56°47.980'		x					
1704	Hydrothermal basalt	A2	28°32.225'	56°48.663'		x					
1714	Tuff	A1	28°28.702'	56°48.841'		x					
1716	Prehnite-clinozoisite vein in basalt	B	28°30.658'	56°50.891'	x						
1717	Gabbro	B	28°30.718'	56°50.878'	x						
1719	Basalt	A4	28°30.774'	56°50.642'		x					
1721	Lawsonite vein in basalt	A2	28°30.217'	56°50.895'	x						
1722	Tuffaceous sandstone	A1	28°30.250'	56°50.447'					x		x
1727	Gabbro	B	28°30.722'	56°51.296'	x				x		
1728	Gabbro	B	28°30.732'	56°51.308'	x				x		
1729	Basalt	B	28°30.745'	56°51.312'	x						
1730	Gabbro	B	28°30.752'	56°51.320'	x						
1731	Gabbro	B	28°30.864'	56°51.443'	x						
1732	Gabbro	B	28°30.852'	56°51.519'		x					
1733	Gabbro	B	28°30.940'	56°51.577'	x						
1734	Gabbro	B	28°31.128'	56°51.525'	x				x		
1735	Basalt	B	28°31.128'	56°51.525'	x						
1736	Lawsonite vein in basalt	B	28°31.133'	56°51.401'	x						
1738	Gabbro	B	28°28.894'	56°52.269'	x						
1745	Gabbro	B	28°28.262'	56°51.895'	x						
pst	Pseudotachylyte	B	28°30.935'	56°51.572'				x			

Abbreviations: Arg—aragonite; blue amp—blue amphibole; EPMA—electron probe microanalyzer; Lws—lawsonite; Raman—Raman spectroscopy on carbonaceous matter; SEM/EDS—scanning electron microscope/energy-dispersive spectroscopy.

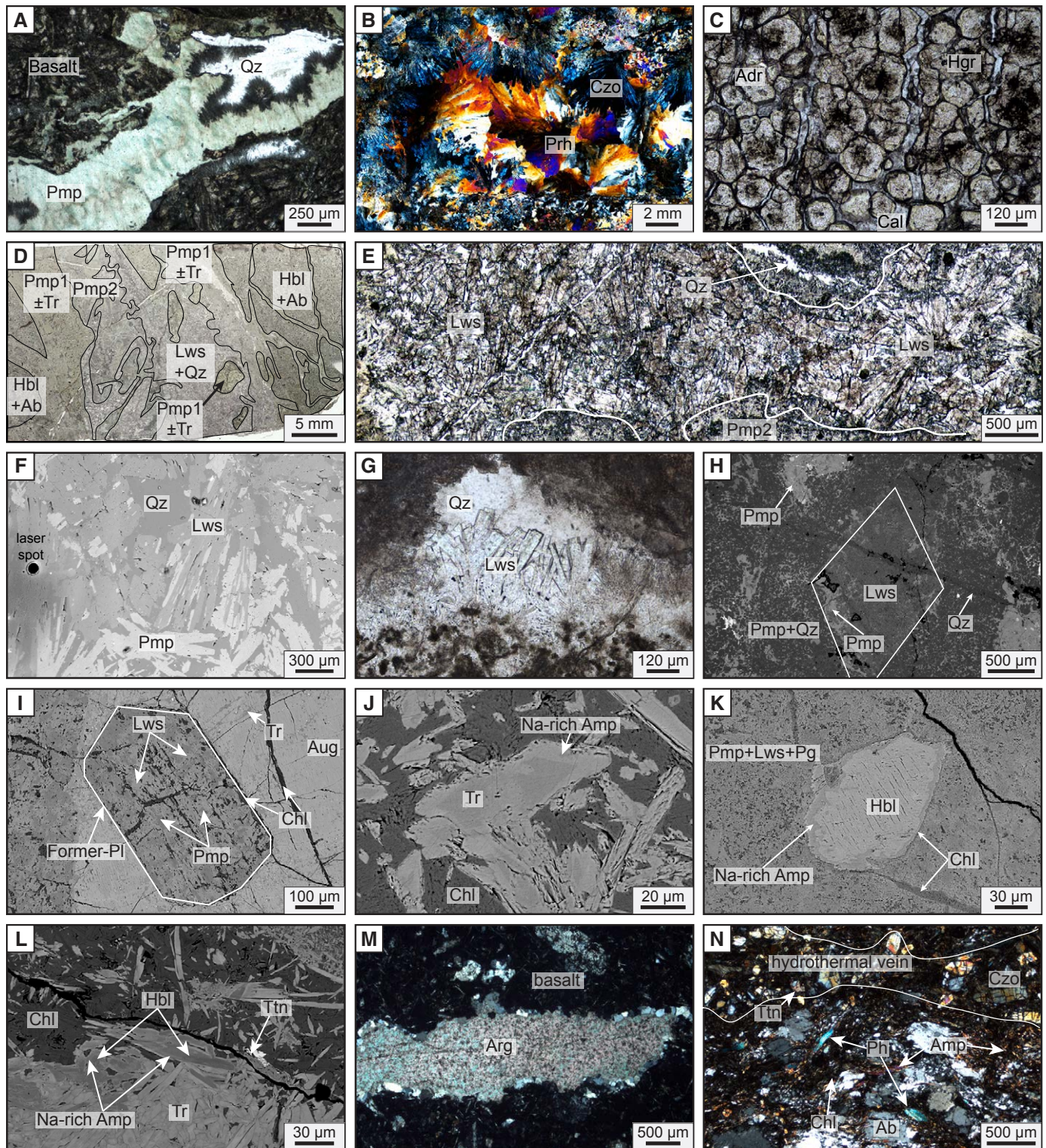


Figure 5. Microphotographs and backscattered electrons images. (A) Pumpellyite-quartz vein in a basalt (1613); (B) prehnite-clinozoisite vein in gabbro (cross-polarized light, 1716); (C) hydroandradite and andradite crystallization in a calc-silicate rock (1603); (D) microstructures of a lawsonite-quartz vein in basalt at the thin-section scale (1529); (E) composite image in a lawsonite-quartz vein in basalt (1529); (F) backscattered electron (BSE) image of a lawsonite-quartz vein, showing destabilization of lawsonite by pumpellyite (1529); (G) small lawsonite-quartz vein in basalt (1607); (H) lawsonite-quartz vein in rhyolite with destabilization of lawsonite into pumpellyite (1518); (I) texture of metagabbro with pristine augite partially replaced by tremolite and plagioclase fully replaced by lawsonite and pumpellyite (1530); (J) overgrowth of Na-rich amphibole over tremolite in gabbro (1530); (K) overgrowth of Na-rich amphibole over hornblende in a high-pressure matrix (1531); (L) complex zoning of amphibole in gabbro (1530); (M) aragonite vein in basaltic rock with quartz-filled vacuoles (1628); and (N) hydrothermal vein crossing a deformed metasediment (1722).

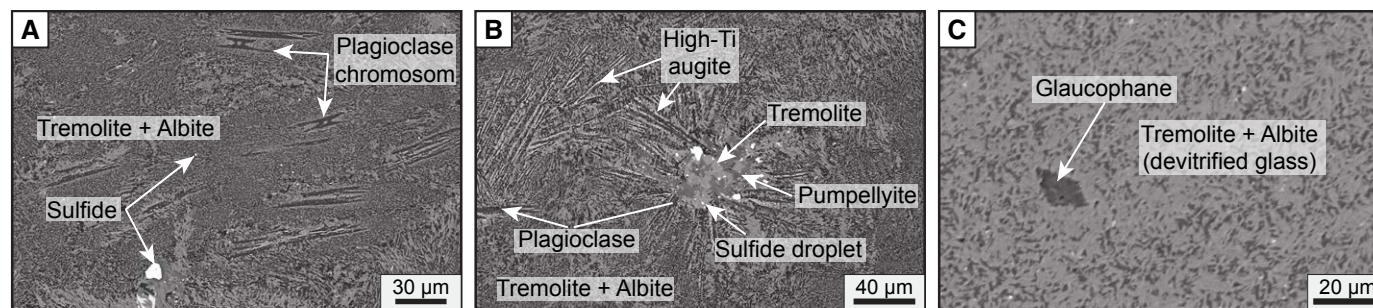


Figure 6. Backscattered electron images of pseudotachylyte vein. (A) Chromosome-shaped plagioclase in a tremolite-albite matrix (devitrified glass) and sulfide; (B) plagioclase-clinopyroxene spherulite; and (C) glaucophane in the tremolite-albite matrix.

TABLE 2. REPRESENTATIVE ANALYSES

Mineral group	Amphibole (core to rim)					Glaucophane		Plagioclase		Fassaite		Phengite			Lawsonite	
	1530	1530	1530	1530	1530	pst	pst	pst	pst	pst	pst	pst	1530	1722	1531	1529
SiO <sub>2</sub>	55.34	42.79	47.76	45.63	52.52	57.10	56.18	53.43	53.73	47.10	49.20	54.35	52.19	50.66	38.97	38.89
TiO <sub>2</sub>	0.12	0.29	0.65	0.58	0.09	-	-	0.17	0.13	1.94	0.66	0.17	0.25	0.20	0.00	0.00
Al <sub>2</sub> O <sub>3</sub>	3.02	15.30	9.26	12.93	4.53	20.12	19.71	26.08	26.59	7.56	8.10	25.28	22.87	26.84	31.93	31.82
Cr <sub>2</sub> O <sub>3</sub>	0.00	0.00	0.00	0.00	0.00	-	-	-	-	-	-	-	0.02	0.04	0.02	0.03
FeO <sub>T</sub>	3.53	7.13	6.29	6.19	6.53	3.71	3.73	1.47	1.29	12.24	13.06	3.26	4.94	3.08	0.17	0.59
MnO	0.06	0.02	0.14	0.08	0.30	-	-	0.06	0.01	0.20	0.24	0.05	0.09	0.03	0.00	0.00
MgO	21.41	16.38	17.71	17.46	19.98	9.32	10.75	1.28	1.46	9.29	14.27	4.07	5.20	3.53	0.12	0.00
CaO	12.75	12.30	12.25	11.81	11.60	0.48	0.47	13.62	12.44	20.80	11.27	0.18	3.49	0.26	18.27	18.41
Na <sub>2</sub> O	0.68	2.78	1.68	2.47	0.75	7.28	7.17	3.54	4.16	0.70	1.32	0.08	1.63	0.49	0.01	0.02
K <sub>2</sub> O	0.05	0.16	0.08	0.13	0.03	-	-	0.10	0.10	0.02	0.13	10.33	6.12	9.13	0.01	0.00
Total	96.96	97.15	95.82	97.29	96.34	98.00	98.00	99.76	99.92	99.85	98.25	97.77	96.80	94.27	89.50	89.76
Si	7.66	6.08	6.83	6.41	7.34	7.53	7.41	2.45	2.45	1.79	1.85	3.53	3.45	3.41	2.02	2.02
Ti	0.01	0.03	0.07	0.06	0.01	-	-	0.01	0.00	0.06	0.02	0.01	0.01	0.01	0.00	0.00
Al	0.49	2.56	1.56	2.14	0.75	3.13	3.06	1.41	1.43	0.34	0.36	1.93	1.78	2.13	1.95	1.94
Cr	0.00	0.00	0.00	0.00	0.00	-	-	0.00	0.00	0.00	-	-	0.00	0.00	0.00	0.00
Fe <sup>3+</sup>	0.19	0.67	0.41	0.67	0.76	0.00	0.00	0.00	0.00	0.03	0.00	0.00	0.00	0.17	0.01	0.03
Fe <sup>2+</sup>	0.22	0.18	0.34	0.06	0.00	0.41	0.41	0.06	0.05	0.36	0.41	0.18	0.27	0.17	0.00	0.00
Mn	0.01	0.00	0.02	0.01	0.00	-	-	0.00	0.00	0.01	0.01	0.00	0.00	0.00	0.00	0.00
Mg	4.42	3.47	3.77	3.66	4.16	1.83	2.11	0.09	0.10	0.53	0.80	0.39	0.51	0.35	0.01	0.00
Ca	1.89	1.87	1.88	1.78	1.74	0.07	0.07	0.67	0.61	0.85	0.45	0.01	0.25	0.02	1.01	1.02
Na	0.18	0.76	0.47	0.67	0.20	1.86	1.83	0.31	0.37	0.05	0.10	0.01	0.21	0.06	0.00	0.00
K	0.01	0.03	0.01	0.02	0.00	-	-	0.01	0.01	0.00	0.01	0.86	0.52	0.78	0.00	0.00
Sum cat	15.08	15.67	15.36	15.47	14.96	14.83	14.89	5.00	5.02	4.01	4.00	6.92	7.00	6.94	5.00	5.01
#(O,OH)	23	23	23	23	23	23	23	8	8	6	6	11	11	11	8	8
	Tr	Mhst	Mhb	Tsch	Mhb	Gln	Gln	An0.68	An0.62							

Abbreviations: cat—cation; Tr—tremolite; Mhst—magnesiostastingsite; Mhb—magnesiornblende; Tsch—tschermakite; Gln—glaucophane; An—anorthite.

### White Mica

White mica is rare overall in Siah Kuh, due to the mainly mafic lithologies, but it is found in metasedimentary sample 1722 and in the pseudotachylyte (Fig. 7A). Core mica in this sample has tetrahedral Si (<sup>3</sup>Si) values of ~3.3 atoms per formula unit (apfu), but rims have higher <sup>3</sup>Si values of ~3.4 and up to 3.52 apfu (Fig. 7A). The pseudotachylyte part of sample 1530 also contains rare white mica with <sup>3</sup>Si of 3.45–3.55 apfu.

### Chlorite

Chlorite is ubiquitous in Siah Kuh mafic and sedimentary rocks. In all lithologies, its composition is clinochlore (Fig. 7B).

### Lawsonite

Lawsonite occurs as veins in metabasalts and as pseudomorphs of plagioclase, with only small compositional differences. Lawsonite crystals in veins are enriched in Fe in the core and rim compared to the mantle (Figs. 7C and 7D). Substitution for aluminum in octahedral sites is very limited (maximum 0.12 apfu on a total of two octahedral sites per eight oxygens), and all points in veins plot on the Cr-Fe<sup>3+</sup> joint of Vitale-Brovarone et al. (2014; see Supplemental Materials<sup>1</sup>). Trace-element patterns (Fig. 7E) show enrichment in Cs, Be, Pb, Sr, Eu, and Ni and a strong depletion in Zr, Hf, Ti, Mn, and Cr and heavy rare-earth elements (HREEs) compared to the primitive mantle, Pb, Sr, and Eu positive anomalies, and Zr, Hf, and Ti negative anomalies. This pattern is similar to what is observed by Martin et al. (2014) and Vitale-Brovarone et al. (2014) but with lower HREE content. Cores of lawsonite have lower REE-Ti concentrations than the rims and a smaller Pb positive anomaly, but higher Sr concentrations.

### Pumpellyite

Pumpellyite is Mg- to Al-pumpellyite (Supplemental Materials [footnote 1]). Higher iron concentrations

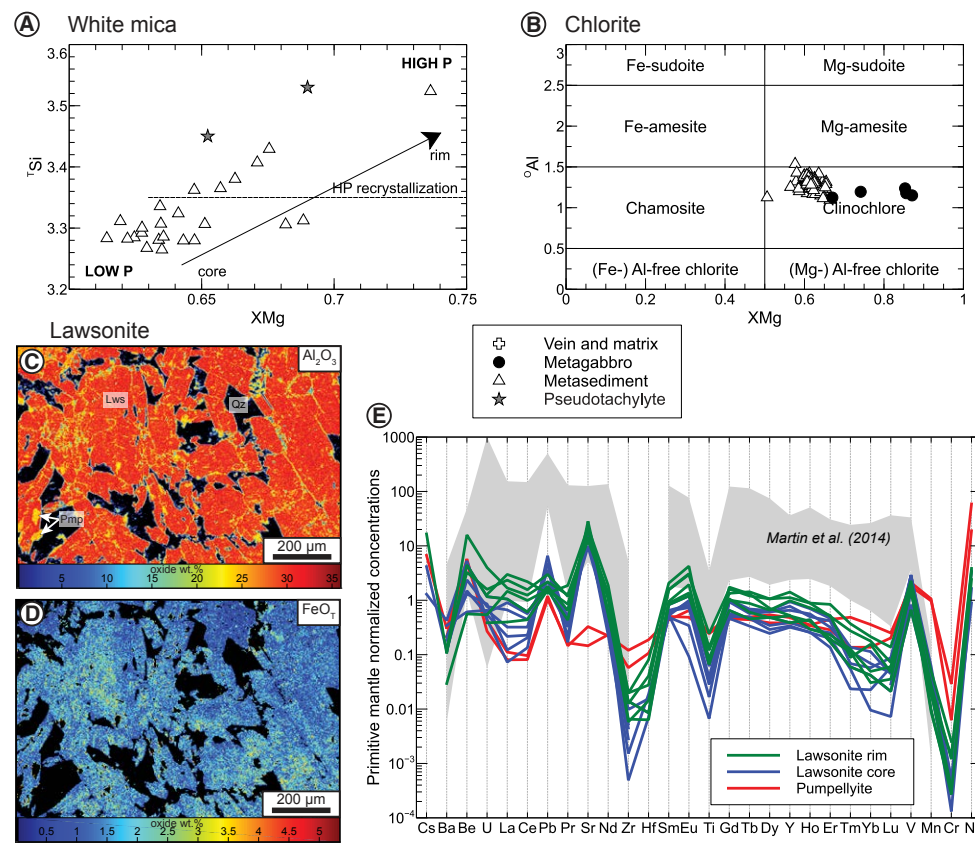


Figure 7. Chemistry of metamorphic minerals. (A) <sup>3</sup>Si versus XMg of white mica; (B) <sup>9</sup>Al versus XMg of chlorite; (C) Al<sub>2</sub>O<sub>3</sub> map of a lawsonite vein (1529); (D) FeO map of lawsonite inside a lawsonite vein (1529); and (E) trace-element patterns of lawsonite in vein.

are observed in prograde pumpellyite compared to retrograde pumpellyite in veins. Prograde pumpellyite is overall poor in rare-earth elements (REEs) but enriched in Cs, Be, V, and Ni compared to the primitive mantle (Fig. 7E). It has positive Pb and Eu anomalies but no Sr anomaly.

### Amphibole

Amphibole is very frequent in metagabbro, where it displays complex zoning as shown by

X-ray maps (Figs. 8A and 8B); this zoning testifies to multi-stage metamorphism. Composition plots (Figs. 8C–8F) show that cores of amphibole have an increasing <sup>4</sup>(Na + K + 2Ca) “pargasitic” content (from tremolite to pargasite), whereas rims have no pargasitic content. In contrast, rims are enriched in <sup>9</sup>Na (sodic ferri-magnesian hornblende). High-Al glaucophane is found within the pseudotachylyte vein. Amphibole in the matrix of lawsonite-quartz veins and in metasediment is tremolite to magnesio-hornblende that shows no sign of high-pressure recrystallization.

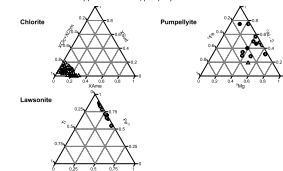
Supplementary materials  
 S1: Striation and fault plane orientation in gabbro  
 S2: Additional chemistry plots for chlorite, pumpellyite and lawsonite  
 S3: Results of Raman spectroscopy on Carbonaceous Material  
 S4: Methods and results of Ar-Ar geochronology  
 S5: Isotopic and age data for Ar-Ar step-heating.

S1: Striation and fault plane orientation in gabbro

Sample	Striation	Fault plane
1	100°	100°
2	100°	100°
3	100°	100°
4	100°	100°
5	100°	100°
6	100°	100°
7	100°	100°
8	100°	100°
9	100°	100°
10	100°	100°
11	100°	100°
12	100°	100°
13	100°	100°
14	100°	100°
15	100°	100°
16	100°	100°
17	100°	100°
18	100°	100°
19	100°	100°
20	100°	100°
21	100°	100°
22	100°	100°
23	100°	100°
24	100°	100°
25	100°	100°
26	100°	100°
27	100°	100°
28	100°	100°
29	100°	100°
30	100°	100°
31	100°	100°
32	100°	100°
33	100°	100°
34	100°	100°
35	100°	100°
36	100°	100°
37	100°	100°
38	100°	100°
39	100°	100°
40	100°	100°
41	100°	100°
42	100°	100°
43	100°	100°
44	100°	100°
45	100°	100°
46	100°	100°
47	100°	100°
48	100°	100°
49	100°	100°
50	100°	100°

Gabbros are located within 50 meters of N28°29.768' E56°51.801'.

S2: Additional chemistry plots for chlorite, pumpellyite and lawsonite



<sup>1</sup>Supplemental Materials. Item S1: Striation and fault plane orientation in gabbro. Item S2: Additional chemistry plots for chlorite, pumpellyite, and lawsonite. Item S3: Results of Raman spectroscopy on carbonaceous material. Item S4: Methods and results of Ar-Ar geochronology. Item S5: Major- and trace-element analyses of lawsonite and pumpellyite. Please visit <https://doi.org/10.1130/GES02134.S1> or access the full-text article on [www.gsapubs.org](http://www.gsapubs.org) to view the Supplemental File.

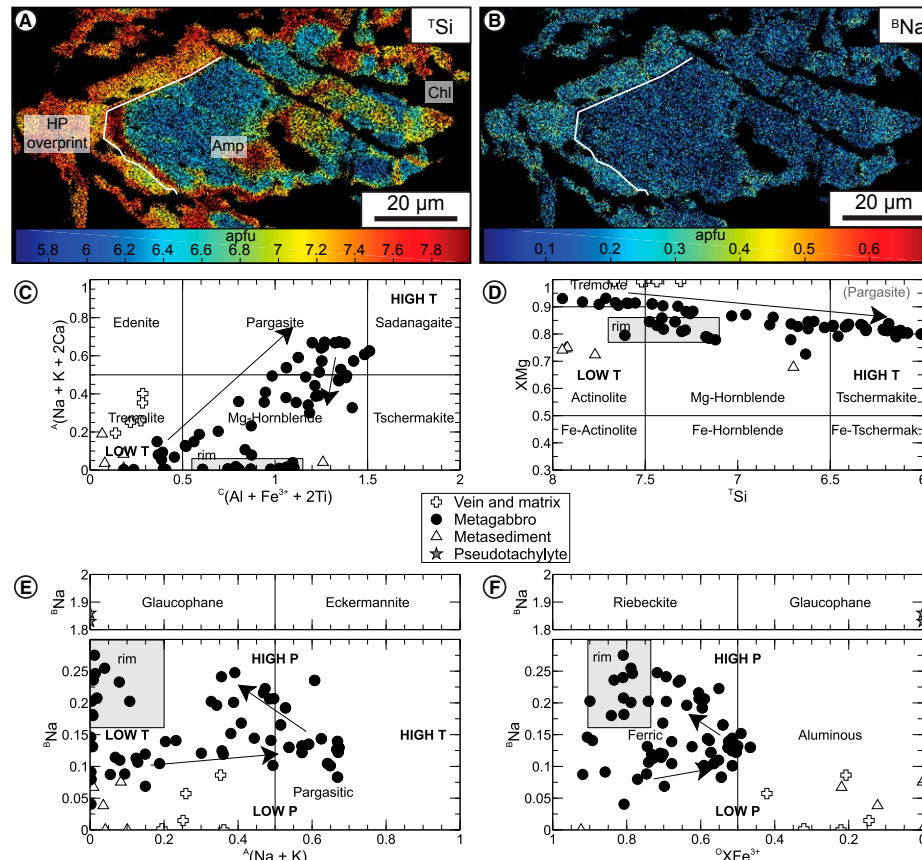


Figure 8. Chemistry of amphiboles. (A) Complex zoning of amphibole revealed by  $^{29}\text{Si}$  mapping, and (B)  $^{23}\text{Na}$  mapping; (C) discrimination diagram of amphibole after Hawthorne et al. (2012); (D) discrimination diagram of amphibole after Leake et al. (1997); (E) plot for amphibole, where  $^{23}\text{Na}$  is a proxy for pressure and  $^{29}\text{Si}$  a proxy for temperature; and (F) plot for amphibole, according to Bonnet et al. (2018).

### Clinopyroxene

Clinopyroxene (other than primary, magmatic augite) is only found within the pseudotachylyte vein. It corresponds to sodium-rich augite with a significant incorporation of Al in the octahedral site and no vacancy, along a Ca-Tschermak substitution ( $\text{Mg, Fe}^{2+} + \text{Si} = 2 \text{ Al}$ ) (Table 2 and Fig. 9A). These analyses are similar to those of clinopyroxene in blueschist-facies pseudotachylytes in Corsica

(Austrheim and Andersen, 2004; Deseta et al., 2014) close to the fassaite described by Deer et al. (2013).

### Plagioclase

Plagioclase (other than magmatic) is found within the pseudotachylyte. It is chemically labradorite, with anorthite fractions from 0.55 to 0.68 (Fig. 9B) but also incorporates up to 0.35 apfu of Fe

and Mg, replacing Al in the tetrahedral site. Charge balance is accommodated by a jadeite-like substitution:  $\text{Na} + \text{Al} = \text{Ca} + (\text{Mg, Fe}^{2+})$ .

### 4.4 P-T Estimates

Precise P-T estimates on low-grade rocks are challenging, due to the existence of only local recrystallizations (i.e., limited rock reactivity). We hence used a multi-step approach to determine approximate P-T conditions in the Siah Kuh edifice.

### Raman Spectroscopy on Carbonaceous Matter

Calibrations used are by Beyssac et al. (2002) for samples 1513 and 1517 and Lahfid et al. (2010) and Kouketsu et al. (2014) for sample 1632. While sample 1632 is a metasediment from within the Siah Kuh seamount, 1513 and 1517 are found on the flanks of Siah Kuh at the limit with the Seghin unit. For sample 1632, all preferred calibrations agree within  $10 \text{ }^\circ\text{C}$  and record a maximum temperature of  $220 \pm 50 \text{ }^\circ\text{C}$  for the core of the seamount.

In contrast, sample 1513 records a maximum temperature of  $500 \text{ }^\circ\text{C}$ , similar to the peak temperatures determined in Seghin (Angiboust et al., 2016).

Sample 1517, located in the sliver between Siah Kuh and the Seghin unit, records a maximum temperature of  $400 \text{ }^\circ\text{C}$ , advocating for peak P-T conditions between Siah Kuh and Seghin.

### Lawsonite Stability

Pseudosection modeling using Perplex v. 6.77 (Connolly, 1990, 2005) has been performed in order to determine the P-T conditions for pure lawsonite formation in quartz-lawsonite veins, using the internally consistent data set of Holland and Powell (2003). Although pumpellyite is present in the veins, it mostly occurs within parts where early hydrothermal veins are reworked and as a retrograde phase destabilizing lawsonite. The starting composition used is the one of lawsonite (equivalent of 1 mol%  $\text{CaO}$ , 1 mol%  $\text{Al}_2\text{O}_3$ ), with quartz

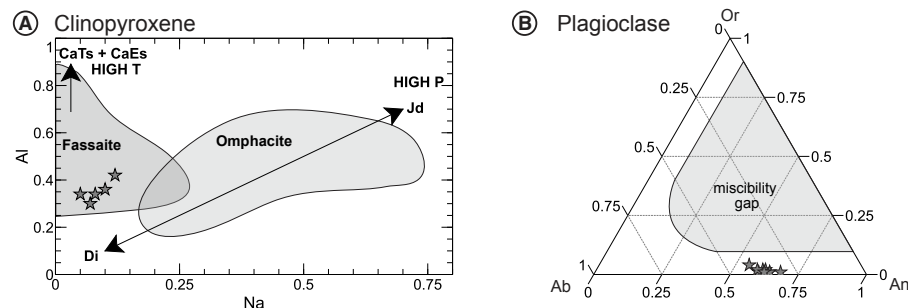


Figure 9. Chemistry of pseudotachylyte minerals. (A) Al versus Na of clinopyroxene. (B) Ternary diagram for plagioclase.

and water saturated. Carbonate minerals are never found in these veins; so the activity of CO<sub>2</sub> was fixed to 0. No solid solutions were used. This pseudo-section model defines a temperature-independent high-pressure field above 0.3 GPa (Fig. 10).

### Aragonite Stability

Pure aragonite in veins in the Siah Kuh seamount can be modeled using the same method, with 1 mol% CaO and saturated CO<sub>2</sub>. This defines a high-pressure-low-temperature domain above 0.6 GPa at 250 °C.

### Absence of Antigorite

The stability of serpentine minerals is highly temperature dependent. In our study, the presence of lizardite and the absence of antigorite and talc point to temperatures below ~300 °C (Evans, 2004; Schwartz et al., 2013).

### Absence of Sodic Pyroxene

Despite the ubiquitous occurrence of pure albite (formed from magmatic plagioclase during hydrothermalism or prograde metamorphism), no pure jadeite has been found in the rocks. This defines a possible high-pressure limitation for the P-T conditions reached by Siah Kuh, below 0.8 GPa

at 250 °C. However, impure jadeite could form at lower pressures, and its absence might point to the low reactivity of rocks.

### Reactions in Metagabbro

Metamorphic textures in metagabbros, as in most rocks from Siah Kuh, are far from equilibrium. The complex zoning pattern is probably inherited from seafloor hydrothermalism, while the <sup>23</sup>Na overprint results from high-pressure metamorphism. Magnesium-rich glaucophane is only found in the devitrified glass of a high-pressure

pseudotachylyte. Recrystallization only concerns rims of pyroxene, shear bands, or plagioclase. In spite of this, element transfer at some stage of the metamorphism must be efficient as shown by open-system plagioclase replacement (influx of Mg, Fe, and H<sub>2</sub>O to form pumpellyite and lawsonite).

The riebeckite-bearing samples of Angiboust et al. (2016) belong to the high-pressure, slightly warmer sliver between Siah Kuh and Seghin; riebeckite was not found anywhere else in the seamount. Glaucophane occurs only in the pseudotachylyte vein.

### Reactions in Metasediment

Most of the metamorphism in metasedimentary sample 1722 seems to be related to low-pressure reactions. Mica cores (and amphiboles) perpendicular to the foliation are supposed to be of detrital origin, as shown by Ar-Ar dating of white mica (age of 123 Ma, older than the underlying limestone; Supplemental Materials [footnote 1]). However, high-<sup>29</sup>Si rims (up to 3.52 apfu) around white mica advocate for a high-pressure record (e.g., Angiboust et al., 2014), although this interpretation might be challenged by the occurrence of pure hydrothermal celadonite on the seafloor (e.g., Alt and Teagle, 2003) and the assemblage missing biotite, K-feldspar, and quartz (Massonne and Schreyer, 1987). We deduce that much of the metamorphic recrystallization within Siah Kuh results from seafloor alteration and relatively high-temperature hydrothermalism, while subduction metamorphism is restricted to only a few index minerals.

Peak P-T conditions for the Siah Kuh seamount can therefore be estimated with temperatures ~220 ± 50 °C and pressures of 0.7 ± 0.1 GPa (Fig. 10).

## 5. DISCUSSION

### 5.1 Seamount Genesis and Oceanic Stage

#### 5.1.1 Seafloor Roughness

Identification of the A unit Siah Kuh as a seamount, i.e., as a discrete volcano on the seafloor is due to (1) the conical shape of the edifice;

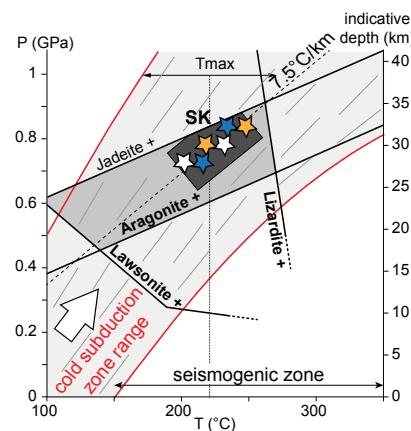


Figure 10. Synthesis of pressure-temperature (P-T) conditions of subduction-related metamorphism for the Siah Kuh (SK) seamount.

(2) voluminous amounts of erupted material building up a continuous, >1.5-km-thick pile of pillow lavas, lava flows, and hyaloclastite; (2) shallow-water column for the sedimentation of massive (possibly reef) limestone on top of this volcanic edifice, with high-energy reworking of sediments and benthic fauna; (3) deepening sediments from shallow-water limestone to pelagic limestone (although the subsidence might not be linked with the load of the seamount; see discussion in 5.1.2); and (4) slope destabilization processes recorded in sediments of the Siah Kuh unit by abundant mass transport deposits (MTDs; such as olistoliths, debris flows, and slumps; Figs. 3F and 3I–3L) affecting diversely consolidated lithologies.

While the current shape of the Siah Kuh unit partly results from thrusting (i.e., B onto A unit) and antiformal arching (Fig. 2), the core of the Siah Kuh unit is relatively unaffected by thrusting and thus probably close to its initial shape.

The large amount of (pillow) lavas is frequently used to characterize seamounts (e.g., Corcoran, 2000). The exposed thickness of the Siah Kuh unit is, however, much less than what is observed in the largest seamounts on Earth (e.g., Hawaii or the Canary islands), where the base lies at ~4–5 km depth and the summit reaches a few km above sea level. The Siah Kuh seamount was, however, not a mid-ocean seamount (with alkaline geochemical signatures) but more likely formed in a supra-subduction environment as an arc volcano (Moghadam et al., 2013). Due to upper-plate bending, the base of arc volcanoes is often situated at shallower depths, ~1.5–3 km (e.g., the Izu-Bonin-Mariana arc, somewhat shallower in the Tonga-Kermadec arc), which is more compatible with the top of the >1.5-km-thick Siah Kuh unit reaching or being close to the surface. More importantly, there are no modern or fossil examples of smooth oceanic crust reaching the ocean surface only due to upper-plate bending.

Given its estimated height, the Siah Kuh seamount would classify among the 10,000 largest seamounts on modern ocean floors (Hillier and Watts, 2007).

The build-up of the core of Siah Kuh is a long-term process, as suggested by the diversity of

volcanic products (basalts and rhyolite) in Siah Kuh. The end of volcanic activity in the core of Siah Kuh is marked by a progressive increase in the amount of sediments with respect to lavas, from mm- to cm-scale sedimentary layers associated with hyaloclastites to tens-of-meters-thick beds of massive limestone deposited at shallow depths intercalated

with lava flows. Whether the seamount reached the surface or not cannot be ascertained by current observations. The absence of massive limestone in the topographically highest portions of the core of Siah Kuh might be due to early erosion or absence of deposition when Siah Kuh was an oceanic island or late erosion during Zagros uplift. In the northern

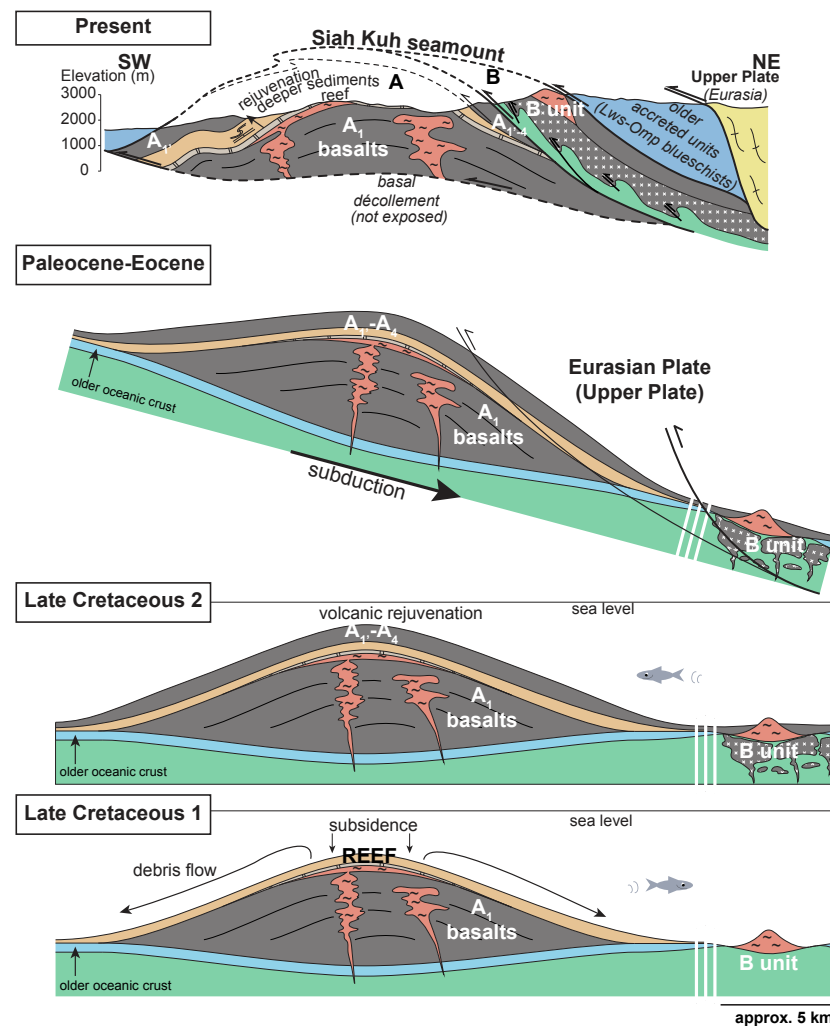


Figure 11. Oceanic and subduction evolution of the Siah Kuh (SK) seamount. Lws-Omp—lawsonite-omphacite.

part of Siah Kuh, pelagic sediments were deposited directly on top of basalts and hyaloclastites from the core of Siah Kuh, thus lacking shallow limestone intercalations. This suggests that the northern portion of the Siah Kuh unit remained at greater depths than its southern counterpart, implying the existence of steep submarine slopes around the summit of the Siah Kuh seamount.

These steep slopes are also suggested by ubiquitous syn-sedimentary mass transport deposits. Similar observations made in modern seamounts and volcanic islands point to the potential tsunamigenic character of these events (e.g., McMurtry et al., 2004).

The B unit is very different because it comprises an ultramafic base and fewer volcanics than the A unit. Initial continuity between the A and B unit is suggested by the occurrence of very similar felsic lavas in A and B and the continuity in metamorphic grades. The scarcity of sediments in B could be explained by a larger sedimentation depth and potential erosion.

While unit B comprises a basal serpentinite enclosing gabbroic pods as part of the oceanic sequence (i.e., below gabbros and basalts), the basement of the A unit is not exposed. Serpentinite pods within thrusts of the A unit suggest it is partly made of serpentinite but may also include older crustal material.

The oceanic evolution of Siah Kuh is presented on Figure 11 (Late Cretaceous).

### 5.1.2 Record of Subsidence in the Siah Kuh Seamount

Sediments within the Siah Kuh seamount show a progression from subsurface (<100 m depth) to pelagic sedimentation (including radiolarian chert commonly forming at several km depth). These sediments are in place directly on top of the seamount, and Cretaceous sea level varies by <100 m (Haq et al., 1987), thus pointing to the subsidence of the whole edifice. Many hypotheses can explain subsidence, such as (1) continuous thermal subsidence of the oceanic plate, (2) thermal subsidence after thermal rejuvenation of the lithosphere, or

(3) isostatic equilibration of the oceanic lithosphere under the load of the seamount. Subsidence could also result from (4) bending of the downgoing plate before subduction (i.e., forebulge and foredeep; Ranero et al., 2003), (5) modifications of asthenospheric mantle upwelling and therefore dynamic topography (Detrick and Crough, 1978), or (6) coupling changes on the subduction interface (Agard et al., 2018).

The Siah Kuh seamount was located close to the Equator during the Late Cretaceous (<15° latitude, Barrier et al., 2008), and the biogenic activity was likely high as were sedimentation rates (>50 m/m.y.; Bosscher and Schlager, 1993). The subsidence must have been faster than sedimentation processes, leading to the drowning of the seamount. This fast subsidence in the Siah Kuh seamount is not compatible with passive processes such as the long-term cooling of the underlying oceanic lithosphere (hypotheses 1 and 2, responsible for a mean subsidence of ~30 m/m.y.; Detrick and Crough, 1978; Smith and Sandwell, 1997) or dynamic topography (hypothesis 5, <50/m.y.; Flament et al., 2013). The large volume of basalt erupted during magmatic rejuvenation, intercalated with pelagic sediments tends to prove that the seamount had a long postsubsidence history that would not be compatible with the forebulge and foredeep hypothesis (hypothesis 4).

We consider hypothesis 3 to be the most likely, because isostatic equilibration of the lithosphere under the load of a seamount is very fast (<1 m.y., Campbell, 1986) and expected to be of the order of several kilometers (e.g., Hawaii, Watts and ten Brink, 1989). The boninites reported in Siah Kuh (Moghadam et al., 2013) also point to an intra-oceanic (and supra-subduction) setting.

Precise dating of the time interval between shallow and deep sedimentation could help quantify subsidence rates and characterize the nature of the oceanic lithosphere, in particular its thermal age (e.g., Smith and Sandwell, 1997).

Resumption of magmatism in Siah Kuh has a limited impact on the subsidence of the oceanic lithosphere (and potential thermal uplift), since only pelagic sediments are interbedded with the lavas.

## 5.2 High-Pressure Metamorphism and Regional Implications

The subduction and later evolution of the Siah Kuh seamount is presented in Figure 11 (from Paleocene–Eocene to present).

### 5.2.1 Pressure-Temperature Conditions and Potential Complexities

Although limited, the metamorphic imprint within Siah Kuh implies peak pressure-temperature conditions of 200–300 °C and 0.5–0.9 GPa. These conditions are typical of high-pressure–low-temperature metamorphism developed in cold geothermal gradients such as subduction zones. The metamorphic imprint (both the density of metamorphic veins and extent of recrystallization) increases toward the NE of Siah Kuh, which is consistent with the past direction of subduction: the deepest subducted units are more metamorphosed. The occurrence of one aragonite vein in the western part of Siah Kuh (sample 1628) implies that pressures above 0.5 GPa are expected even for the shallowest part. Hence, the whole Siah Kuh seamount was subducted down to 20–30 km.

A comparable trend in metamorphic conditions is observed in the Anarak seamount (Bagheri and Stampfli, 2008). This evolution of metamorphism could correspond to the depth difference between the front and the back of a subducted seamount (~7 km, ~0.2 GPa, and 40 °C for the Siah Kuh seamount on a 20° dip slab). An alternative explanation for this metamorphic trend involves tectonic overpressure and underpressure (Gerya, 2015; Ruh et al., 2017), but this would result in estimated pressure differences between the front and back of the subducting seamount ≤0.2 GPa.

The increasing density of metamorphic veins toward the deepest parts requires the occurrence of brittle failure, which in theory is impeded by increased confining pressure, and requires an excess of either shear stress (i.e., tectonic overpressure) or pore-fluid pressure (i.e., fluid overpressure leading to hydraulic brecciation). The apparently random vein orientation in Siah Kuh favors the

second hypothesis. This observation and lawsonite crystallization in gabbro exclusively in the northeast part of Siah Kuh could be explained by warmer temperatures that increase the solubility of solutes in super-critical metamorphic fluids. Fast exhumation of the Siah Kuh unit is required to allow the preservation of fresh metamorphic aragonite and lawsonite (Gillet and Goffé, 1988).

### 5.2.2 Regional Significance

The Siah Kuh seamount is one of the few remnants of Neotethyan oceanic lithosphere subducted below Eurasia (which later evolved into the Zagros collision; Agard et al., 2006, 2011). Given its structural position below subducted units (oceanic and offscraped from the slab or as part of a forearc, i.e., the Seghin and Ashin units, respectively; Angiboust et al., 2016), it can be concluded that Siah Kuh was located outboard of Eurasia, as part of the lower plate with respect to the Eurasian subduction zone. The presence of boninites (Moghadam et al., 2013) suggests that the Siah Kuh seamount was also in a supra-subduction position with respect to a second, more southerly subduction (which is well documented by regional studies; e.g., Searle and Cox, 1999; Agard et al., 2006, 2007). Due to its structural position below the Ashin unit and the Seghin blueschists, the Siah Kuh unit most likely underwent subduction and metamorphism after them. The age of oceanic sediments overlying Siah Kuh is Upper Campanian to Maastrichtian (76–66 Ma, Sabzehei, 1974), making it indeed younger than almost all metamorphic ages in the Ashin and Seghin units. Subduction of the Siah Kuh seamount may have favored the final exhumation of older blueschist units in the Hajiabad-Esfandagheh area because it represents a more buoyant piece of slab (Cloos, 1993). The 123 Ma age of white mica in Siah Kuh metasediments, in any case, does not constrain the timing of metamorphism, because the ages are older than sedimentation in the Siah Kuh unit (76–66 Ma) and may correspond to detrital micas showing an age mixing between earlier and high-pressure metamorphism (Fig. 7A).

## 5.3 Implications for Subduction Interface Processes

### 5.3.1 Location at the Subduction Interface

The Siah Kuh seamount was subducted down to ~30 km. While the top of Siah Kuh clearly was at the top of the slab (i.e., along the subduction interface; Agard et al., 2018), the nature of the upper plate is debatable. The present-day Seghin unit and the small intermediate sliver thrust onto Siah Kuh are, however, good candidates. This is suggested by the greater abundance of low  $^{31}\text{Si}$  phengite crystals in samples from the bottom part of the Seghin unit (Angiboust et al., 2016); these crystals may reflect the juxtaposition with the Siah Kuh unit. Chaotic metamorphic blueschist-facies lineation in parts of the Seghin unit could reflect postlineation disturbance by the subducting Siah Kuh seamount (Fig. 1D). There are, however, no clues for major tectonic erosion of the Seghin unit due to subduction of the Siah Kuh seamount (Vannucchi et al., 2006; Clarke et al., 2018).

### 5.3.2 Strain Localization

Subduction-related deformation is mostly localized in serpentinite between the A and the B unit, and in sediments (with minor serpentinite) below magmatic rejuvenation events of the A unit. This deformation migrates from within the A unit to the contact between the A and B units, as shown by faults within the A unit that are crosscut by the major thrust fault separating A from B. Small offsets (maximum hectometric) are observed within the A unit, while kilometer-scale offsets are observed between the A and the B unit. By contrast, the later, Neogene deformation is highlighted by the folding of the reef limestone, which is likely related to the activity of a collisional blind thrust below Siah Kuh.

Most of the deformation within A and B is ductile: pressure solution seams in sediments, subgrain formation, twinning and moderate dynamic recrystallization in calcite, incipient bulging and undulose extinction of quartz, and growth of phyllosilicate

along grain boundaries (this study; Angiboust et al., 2016). Brittle deformation is rather observed in veins (mainly lawsonite veins) within the A unit, in cataclastic gabbros and in one pseudotachylite vein in the B unit.

The long-term tectonic evolution of Siah Kuh unit suggests that (1) the main subduction interface was initially located above the seamount (Fig. 11), with incipient deformation localizing within the A unit, ultimately leading to the detachment of the seamount from the slab (2) at peak burial, the main subduction interface was locked, and the A and B units juxtaposed (with some evidence for brittle deformation, as discussed above), and (3) ductile deformation prevailed during and after detachment of the seamount from the downgoing slab around peak metamorphic conditions. Detachment must be in part rooted in the serpentinized mantle, as shown by the occurrence of serpentinite within faults (basal serpentinite of the B unit and serpentinite pods within the A unit). The interface might also be the contact between oceanic lithosphere underlying the seamount, because this has been shown to be a weak layer where deformation is localized (e.g., in Hawaii; Got et al., 2008). The complex nature of the Neotethyan lithosphere (potentially involving extensional continental allochthons) can also favor this detachment.

### 5.3.3 Seismogenic Behavior

The Siah Kuh seamount was subducted down to ~30 km at ~250 °C, i.e., within the subduction seismogenic zone (Hyndman et al., 1997). Fossil earthquake rocks in subduction contexts are diverse since they depend on strain rate, from high strain rate frictional melting creating pseudotachylites to intermediate strain rates involving small slip on thick fault zones (e.g., Rowe et al., 2011; Angiboust et al., 2015). Pseudotachylites are rare in exhumed units, possibly due to alteration (Kirkpatrick and Rowe, 2013), but examples of subduction-related ones are found in metasediments (e.g., Ikesawa et al., 2003), around the Moho of the subducted plate (e.g., Corsica: Austrheim and Andersen, 2004; Andersen et al., 2014; Deseta et al., 2014; Magott

et al., 2016; Lanzo Massif, W. Alps: Scambelluri et al., 2017) or within subducted continental crust (e.g., pseudotachylyte and breccia, Austrheim and Boundy, 1994; Menant et al., 2018).

The decameter-to-hectometer-long pseudotachylyte vein in the gabbros of the B unit records one fracturing event with centimeter-to-decimeter-scale slip at high strain rate (hence possibly recording a single Mw~2–3 earthquake). The crystallization of fassaitic clinopyroxene from the melt indicates that frictional melting of the host gabbro occurred under high-pressure conditions (Wenk and Weiss, 1982; Spray, 1988; Austrheim and Andersen, 2004; Deseta et al., 2014). The rest of the pseudotachylyte, initially made of glass, was completely devitrified into (1) glaucophane and phengite at high pressure and (2) tremolite and albite at lower pressure. There is, however, no record of larger magnitude earthquakes nucleated within the seamount that would involve networks of thicker pseudotachylyte veins.

The occurrence of such a small earthquake is reminiscent of what has been observed around the Moho of the subducting plate in Corsica (Andersen et al., 2014; Magott et al., 2016) and probably represents an analog of the low-magnitude earthquakes detected in present-day subduction zones.

Cataclastic deformation along grain boundaries (~1cm<sup>2</sup>) in gabbros at the base of B could be late, but striation agrees with subduction convergence direction. Whether these could correspond to small magnitude earthquakes with complex rupture properties and/or low-frequency earthquakes or seismic tremor (Fagereng et al., 2011) is completely unknown but could be further studied. In contrast, sediments within Siah Kuh experience mainly ductile deformation that would be associated with creep (Fagereng and den Hartog, 2017).

Variations in fluid pressure are also critical to generate or impede subduction earthquakes. While high pore-fluid pressure facilitates small-scale rupture and creep processes (e.g., Kodaira et al., 2004; Wang and Bilek, 2014), low pore-fluid pressure can favor the accumulation of stress in faults that can ultimately lead to large earthquakes. Geophysical and seismic imaging suggests high pore-fluid pressure along the subduction interface, in particular in and at the front of seamounts, which is commonly

used to infer a mainly aseismic behavior of seamounts (Mochizuki et al., 2008; Bell et al., 2010; Kato et al., 2010). High-pressure veins in Siah Kuh attest to the existence of high-fluid pressures responsible for the fracture and brecciation of the surrounding rocks. The absence of major slip within these veins suggests that shear stress does not build up, possibly due to high pore-fluid pressures.

All these observations indicate that the Siah Kuh seamount never behaved as a mega-earthquake asperity, and possibly impeded earthquake propagation.

### 5.3.4 Fluid Circulation in the Seismogenic Zone

Fluid has a very strong influence on the creeping and seismogenic properties of subducted materials. Examining the origin of fluid (using geochemical tools) is therefore critical.

High-pressure veins in the Siah Kuh seamount are markers for fluid circulation in the seismogenic zone (Fig. 12). They relate to a minimum of two different fluids, one responsible for lawsonite veins and another one that forms aragonite veins.

Geochemical data on lawsonite in this paper are the first to be published in these kinds of

lithologies and metamorphic grade (for deeper examples: Martin et al., 2014; Vitale-Brovarone et al., 2014). Progressive enrichment of lawsonite in REE from core to rim suggests a continuous fluid circulation and open-system crystallization and potential dissolution-precipitation mechanisms. This, however, involves a single source, as attested to by the similarity of all spectra. A more detailed work, focusing on different veins within the Siah Kuh seamount could help decipher whether the fluid signature is homogeneous or not at a larger scale and potentially trace the origin of these fluids.

The higher density of lawsonite veins in the deepest subducted part of Siah Kuh supports local dehydration, brecciation, and reprecipitation.

## 6. CONCLUSIONS

The Siah Kuh unit is an exceptionally preserved and fully exposed seamount in the Zagros suture zone. Our study reveals the complete history recorded by this average-sized seamount (~12 × 20 km, ~3 km high). The main volcanic activity occurred during the Late Cretaceous and formed a bathymetric relief, a seamount, or possibly an oceanic island. Simultaneous fast subsidence and slope

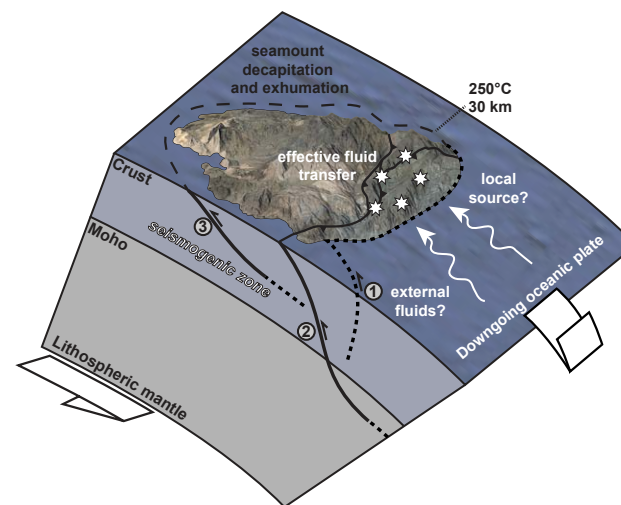


Figure 12. Provenance of fluids in the Siah Kuh seamount. Local or deep source?

instabilities anomaly are followed by a resumption of volcanism. This edifice was subducted down to ~30 km during Paleocene–Eocene, and deformation is mainly localized within the structural heterogeneities of the seamount. There is no proof for a large subduction earthquake through the Siah Kuh unit, which suggests that it did not behave as a seismogenic asperity (and even possibly behaved as a barrier to earthquakes). Metamorphic veins record subduction-related fluid circulation within the seamount. These results (1) constrain the long-standing geological evolution of an exceptionally preserved subducted seamount; (2) document the mechanical and chemical transformations of a seamount during subduction at lower blueschist-facies conditions; and (3) show how fluids migrate in the slab during subduction.

#### ACKNOWLEDGMENTS

This study was partly funded by the project “Zooming in between plates” (Marie Curie International Training Network no. 604713) to P. Agard and by IDEX grant #16C538 to S. Angiboust. We thank the Geological Survey of Iran for assistance in the field and E. Delairis, O. Boudouma, M. Fialin, N. Rividi, and D. Deldicque for technical and analytical support. Special thanks to S. Guillot, J. Escartin, F. Rossetti, F. Meneghini, L. Jolivet, and to the ZIP and E-FIRE scientists for insightful discussions. The manuscript benefited from the useful suggestions of two anonymous reviewers, Guest Associate Editor G. Bebout and Science Editor S. de Silva.

#### REFERENCES CITED

- Agard, P., Omrani, J., Jolivet, L., and Mouthereau, F., 2005, Convergence history across Zagros (Iran): Constraints from collisional and earlier deformation: *International Journal of Earth Sciences*, v. 94, p. 401–419, <https://doi.org/10.1007/s00531-005-0481-4>.
- Agard, P., Monié, P., Gerber, W., Omrani, J., Molinaro, M., Meyer, B., Labrousse, L., Vrielynck, B., Jolivet, L., and Yamato, P., 2006, Transient, synobduction exhumation of Zagros blueschists inferred from P-T, deformation, time, and kinematic constraints: Implications for Neotethyan wedge dynamics: *Journal of Geophysical Research*, v. 111, B11401, <https://doi.org/10.1029/2005JB004103>.
- Agard, P., Jolivet, L., Vrielynck, B., Buron, E., and Monié, P., 2007, Plate acceleration: The obduction trigger?: *Earth and Planetary Science Letters*, v. 258, p. 428–441, <https://doi.org/10.1016/j.epsl.2007.04.002>.
- Agard, P., Omrani, J., Jolivet, L., Whitechurch, H., Vrielynck, B., Spakman, W., Monié, P., Meyer, B., and Wortel, M.J.R., 2011, Zagros orogeny: A subduction-dominated process: *Geological Magazine*, v. 148, p. 692–725, <https://doi.org/10.1017/S001675681100046X>.

- Agard, P., Plunder, A., Angiboust, S., Bonnet, G., and Ruh, J.B., 2018, The subduction plate interface: Rock record and mechanical coupling (from long to short timescales): *Lithos*, v. 320–321, p. 537–566, <https://doi.org/10.1016/j.lithos.2018.09.029>.
- Alt, J.C., and Teagle, D.A.H., 2003, Hydrothermal alteration of upper oceanic crust formed at a fast-spreading ridge: Mineral, chemical, and isotopic evidence from ODP Site 801: *Chemical Geology*, v. 201, p. 191–211, [https://doi.org/10.1016/S0009-2541\(03\)00201-8](https://doi.org/10.1016/S0009-2541(03)00201-8).
- Andersen, T.B., Austrheim, H., Deseta, N., Silkoset, P., and Ashwal, L.D., 2014, Large subduction earthquakes along the fossil Moho in Alpine Corsica: *Geology*, v. 42, p. 395–398, <https://doi.org/10.1130/G35345.1>.
- Angiboust, S., Glodny, J., Oncken, O., and Chopin, C., 2014, In search of transient subduction interfaces in the Dent Blanche–Sesia Tectonic System (W. Alps): *Lithos*, v. 205, p. 298–321, <https://doi.org/10.1016/j.lithos.2014.07.001>.
- Angiboust, S., Kirsch, J., Oncken, O., Glodny, J., Monié, P., and Rybacki, E., 2015, Probing the transition between seismically coupled and decoupled segments along an ancient subduction interface: *Geochemistry Geophysics Geosystems*, v. 16, p. 1905–1922, <https://doi.org/10.1002/2015GC005776>.
- Angiboust, S., Agard, P., Glodny, J., Omrani, J., and Oncken, O., 2016, Zagros blueschists: Episodic underplating and long-lived cooling of a subduction zone: *Earth and Planetary Science Letters*, v. 443, p. 48–58, <https://doi.org/10.1016/j.epsl.2016.03.017>.
- Austrheim, H., and Andersen, T.B., 2004, Pseudotachylytes from Corsica: Fossil earthquakes from a subduction complex: *Terra Nova*, v. 16, p. 193–197, <https://doi.org/10.1111/j.1365-3121.2004.00551.x>.
- Austrheim, H., and Boundy, T.M., 1994, Pseudotachylytes generated during seismic faulting and eclogitization of the deep crust: *Science*, v. 265, p. 82–83, <https://doi.org/10.1126/science.265.5168.82>.
- Bagheri, S., and Stampfli, G.M., 2008, The Anarak, Jandaq and Posht-e-Badam metamorphic complexes in central Iran: New geological data, relationships and tectonic implications: *Tectonophysics*, v. 451, p. 123–155, <https://doi.org/10.1016/j.tecto.2007.11.047>.
- Barrier, E., Vrielynck, B., Bergerat, F., Brunet, M.-F., Mosar, J., Poisson, A., and Sosson, M., 2008, Palaeotectonic maps of the Middle East: Tectono-sedimentary-palinspastic maps from Late Norian to Pliocene Atlas of 14 Maps: Paris, Commission de la carte géologique du monde.
- Bell, R., Sutherland, R., Barker, D.H.N., Henrys, S., Bannister, S., Wallace, L.M., and Beavan, J., 2010, Seismic reflection character of the Hikurangi subduction interface, New Zealand, in the region of repeated Gisborne slow slip events: *Geophysical Journal International*, v. 180, p. 34–48, <https://doi.org/10.1111/j.1365-246X.2009.04401.x>.
- Beyssac, O., Goffé, B., Chopin, C., and Rouzaud, J.-N., 2002, Raman spectra of carbonaceous material in metasediments: A new geothermometer: *Journal of Metamorphic Geology*, v. 20, p. 859–871, <https://doi.org/10.1046/j.1525-1314.2002.00408.x>.
- Bonnet, G., Agard, P., Angiboust, S., Monié, P., Jentzer, M., Omrani, J., Whitechurch, H., and Fournier, M., 2018, Tectonic slicing and mixing processes along the subduction interface: The Sistan example (Eastern Iran): *Lithos*, v. 310–311, p. 269–287, <https://doi.org/10.1016/j.lithos.2018.04.016>.
- Bonnet, G., Agard, P., Angiboust, S., Fournier, M., and Omrani, J., 2019, No large earthquakes in fully exposed subducted seamount: *Geology*, v. 47, p. 407–410, <https://doi.org/10.1130/G45564.1>.
- Bosscher, H., and Schlager, W., 1993, Accumulation rates of carbonate platforms: *The Journal of Geology*, v. 101, p. 345–355, <https://doi.org/10.1086/648228>.
- Campbell, J.F., 1986, Subsidence rates for the Southeastern Hawaiian Islands determined from submerged terraces: *Geo-Marine Letters*, v. 6, p. 139–146, <https://doi.org/10.1007/BF02238084>.
- Clarke, A.P., Vannucchi, P., and Morgan, J., 2018, Seamount chain–subduction zone interactions: Implications for accretionary and erosive subduction zone behavior: *Geology*, v. 46, p. 367–370, <https://doi.org/10.1130/G40063.1>.
- Cloos, M., 1992, Thrust-type subduction-zone earthquakes and seamount asperities: A physical model for seismic rupture: *Geology*, v. 20, p. 601–604, [https://doi.org/10.1130/0091-7613\(1992\)020<0601:TTSZEA>2.3.CO;2](https://doi.org/10.1130/0091-7613(1992)020<0601:TTSZEA>2.3.CO;2).
- Cloos, M., 1993, Lithospheric buoyancy and collisional orogenesis: Subduction of oceanic plateaus, continental margins, island arcs, spreading ridges, and seamounts: *Geological Society of America Bulletin*, v. 105, p. 715–737, [https://doi.org/10.1130/0016-7606\(1993\)105<0715:LBACOS>2.3.CO;2](https://doi.org/10.1130/0016-7606(1993)105<0715:LBACOS>2.3.CO;2).
- Cloos, M., and Shreve, R.L., 1996, Shear zone thickness and the seismicity of Chilean- and Mariana-type subduction zones: *Geology*, v. 24, p. 107–110, [https://doi.org/10.1130/0091-7613\(1996\)024<0107:SZTATS>2.3.CO;2](https://doi.org/10.1130/0091-7613(1996)024<0107:SZTATS>2.3.CO;2).
- Connolly, J.A.D., 1990, Multivariable phase diagrams: An algorithm based on generalized thermodynamics: *American Journal of Science*, v. 290, p. 666–718, <https://doi.org/10.2475/ajs.290.6.666>.
- Connolly, J.A.D., 2005, Computation of phase equilibria by linear programming: A tool for geodynamic modeling and its application to subduction zone decarbonation: *Earth and Planetary Science Letters*, v. 236, p. 524–541, <https://doi.org/10.1016/j.epsl.2005.04.033>.
- Corcoran, P.L., 2000, Recognizing distinct portions of seamounts using volcanic facies analysis: Examples from the Archean Slave Province, NWT, Canada: *Precambrian Research*, v. 101, p. 237–261, [https://doi.org/10.1016/S0301-9268\(99\)00090-X](https://doi.org/10.1016/S0301-9268(99)00090-X).
- Deer, W.A., Howie, R.A., and Zussman, J., 2013, *An Introduction to Rock-Forming Minerals* (3rd ed.): London, The Mineralogical Society, 498 p.
- Delaloye, M., and Desmons, J., 1980, Ophiolites and mélange terranes in Iran: A geochronological study and its paleotectonic implications: *Tectonophysics*, v. 68, p. 83–111, [https://doi.org/10.1016/0040-1951\(80\)90009-8](https://doi.org/10.1016/0040-1951(80)90009-8).
- De La Pierre, M., Carteret, C., Maschio, L., André, E., Orlando, R., and Dovesi, R., 2014, The Raman spectrum of CaCO<sub>3</sub> polymorphs calcite and aragonite: A combined experimental and computational study: *The Journal of Chemical Physics*, v. 140, p. 164,509, <https://doi.org/10.1063/1.4871900>.
- Deseta, N., Ashwal, L.D., and Andersen, T.B., 2014, Initiating intermediate-depth earthquakes: Insights from a HP–LT ophiolite from Corsica: *Lithos*, v. 206–207, p. 127–146, <https://doi.org/10.1016/j.lithos.2014.07.022>.
- Detrick, R.S., and Crough, S.T., 1978, Island subsidence, hot spots, and lithospheric thinning: *Journal of Geophysical Research*, v. 83, p. 1236, <https://doi.org/10.1029/JB083iB03p01236>.
- Evans, B.W., 2004, The Serpentinite Multisystem Revisited: Chrysotile Is Metastable: *International Geology Review*,

- v. 46, p. 479–506, <https://doi.org/10.2747/0020-6814.46.6.479>.
- Fagereng, Å., and den Hartog, S.A.M., 2017, Subduction megathrust creep governed by pressure solution and frictional-viscous flow: *Nature Geoscience*, v. 10, p. 51–57, <https://doi.org/10.1038/ngeo2857>.
- Fagereng, Å., Remitti, F., and Sibson, R.H., 2011, Incrementally developed slickenfibers—Geological record of repeating low stress-drop seismic events?: *Tectonophysics*, v. 510, p. 381–386, <https://doi.org/10.1016/j.tecto.2011.08.015>.
- Flament, N., Gurnis, M., and Müller, R.D., 2013, A review of observations and models of dynamic topography: *Lithosphere*, v. 5, p. 189–210, <https://doi.org/10.1130/L245.1>.
- Gansser, A., 1955, 2. New Aspects of the Geology in Central Iran (Iran), in *World Petroleum Congress*, p. 279–300.
- Geersen, J., Ranero, C.R., Barckhausen, U., and Reichert, C., 2015, Subducting seamounts control interplate coupling and seismic rupture in the 2014 Iquique earthquake area: *Nature Communications*, v. 6, p. 8267, <https://doi.org/10.1038/ncomms9267>.
- Gerya, T., 2015, Tectonic overpressure and underpressure in lithospheric tectonics and metamorphism: *Journal of Metamorphic Geology*, v. 33, p. 785–800, <https://doi.org/10.1111/jmg.12144>.
- Gillet, P., and Goffé, B., 1988, On the significance of aragonite occurrences in the Western Alps: *Contributions to Mineralogy and Petrology*, v. 99, p. 70–81, <https://doi.org/10.1007/BF00399367>.
- Got, J.-L., Montellier, V., Monteux, J., Hassani, R., and Okubo, P., 2008, Deformation and rupture of the oceanic crust may control growth of Hawaiian volcanoes: *Nature*, v. 451, p. 453–456, <https://doi.org/10.1038/nature06481>.
- Groppo, C., Rinaudo, C., Cairo, S., Gastaldi, D., and Compagnoni, R., 2006, Micro-Raman spectroscopy for a quick and reliable identification of serpentine minerals from ultramafics: *European Journal of Mineralogy*, v. 18, p. 319–329, <https://doi.org/10.1127/0935-1221/2006/0018-0319>.
- Haq, B.U., Hardenbol, J., and Vail, P.R., 1987, Chronology of fluctuating sea levels since the Triassic: *Science*, v. 235, p. 1156–1167, <https://doi.org/10.1126/science.235.4793.1156>.
- Hawthorne, F.C., Oberti, R., Harlow, G.E., Maresch, W.V., Martin, R.F., Schumacher, J.C., and Welch, M.D., 2012, IMA report: Nomenclature of the amphibole supergroup: *The American Mineralogist*, v. 97, p. 2031–2048, <https://doi.org/10.2138/am.2012.4276>.
- Hillier, J.K., and Watts, A.B., 2007, Global distribution of seamounts from ship-track bathymetry data: *Geophysical Research Letters*, v. 34, L13304, <https://doi.org/10.1029/2007GL029874>.
- Holland, T.J.B., and Powell, R., 2003, Activity-compositions relations for phases in petrological calculations: An asymmetric multicomponent formulation: *Contributions to Mineralogy and Petrology*, v. 145, p. 492–501, <https://doi.org/10.1007/s00410-003-0464-z>.
- Hyndman, R.D., Yamano, M., and Oleskevich, D.A., 1997, The seismogenic zone of subduction thrust faults: *The Island Arc*, v. 6, p. 244–260, <https://doi.org/10.1111/j.1440-1738.1997.tb00175.x>.
- Ikesawa, E., Sakaguchi, A., and Kimura, G., 2003, Pseudotachylite from an ancient accretionary complex: Evidence for melt generation during seismic slip along a master décollement?: *Geology*, v. 31, p. 637, [https://doi.org/10.1130/0091-7613\(2003\)031<0637:PFAAAC>2.0.CO;2](https://doi.org/10.1130/0091-7613(2003)031<0637:PFAAAC>2.0.CO;2).
- Jochum, K.P., Willbold, M., Raczek, I., Stoll, B., and Herwig, K., 2005, Chemical Characterization of the USGS Reference Glasses GSA-1G, GSC-1G, GSD-1G, GSE-1G, BCR-2G, BHVO-2G and BIR-1G Using EPMA, ID-TIMS, ID-ICP-MS and LA-ICP-MS: *Geostandards and Geoanalytical Research*, v. 29, p. 285–302, <https://doi.org/10.1111/j.1751-908X.2005.tb00901.x>.
- Kato, A., Iidaka, T., Ikuta, R., Yoshida, Y., Katsumata, K., Iwasaki, T., Sakai, S., Thurber, C., Tsumura, N., Yamaoka, K., Watanabe, T., Kunitomo, T., Yamazaki, F., Okubo, M., Suzuki, S., and Hirata, N., 2010, Variations of fluid pressure within the subducting oceanic crust and slow earthquakes: *Geophysical Research Letters*, v. 37, <https://doi.org/10.1029/2010GL043723>.
- Keating, B.H., and McGuire, W., 2000, Island edifice failures and associated tsunami hazards: *Pure and Applied Geophysics*, v. 157, p. 899–955, <https://doi.org/10.1007/s000240050011>.
- Kelleher, J., and McCann, W., 1976, Buoyant zones, great earthquakes, and unstable boundaries of subduction: *Journal of Geophysical Research*, v. 81, p. 4885–4896, <https://doi.org/10.1029/JB081i026p04885>.
- Kirkpatrick, J.D., and Rowe, C.D., 2013, Disappearing ink: How pseudotachylites are lost from the rock record: *Journal of Structural Geology*, v. 52, p. 183–198, <https://doi.org/10.1016/j.jsg.2013.03.003>.
- Kodaira, S., Iidaka, T., Kato, A., Park, J.-O., Iwasaki, T., and Kaneda, Y., 2004, High pore fluid pressure may cause silent slip in the Nankai Trough: *Science*, v. 304, p. 1295–1298, <https://doi.org/10.1126/science.1096535>.
- Kouketsu, Y., Mizukami, T., Mori, H., Endo, S., Aoya, M., Hara, H., Nakamura, D., and Wallis, S., 2014, A new approach to develop the Raman carbonaceous material geothermometer for low-grade metamorphism using peak width: *Raman CM geothermometer using FWHM: The Island Arc*, v. 23, p. 33–50, <https://doi.org/10.1111/iar.12057>.
- Lahfid, A., Beyssac, O., Deville, E., Negro, F., Chopin, C., and Goffé, B., 2010, Evolution of the Raman spectrum of carbonaceous material in low-grade metasediments of the Glarus Alps (Switzerland): *Terra Nova*, v. 22, p. 354–360, <https://doi.org/10.1111/j.1365-3121.2010.00956.x>.
- Lallemant, S., Peyret, M., van Rijnsingen, E., Arcay, D., and Heuret, A., 2018, Roughness characteristics of oceanic seafloor prior to subduction in relation to the seismogenic potential of subduction zones: *Geochemistry, Geophysics, Geosystems*, v. 19, p. 2121–2146, <https://doi.org/10.1029/2018GC007434>.
- Lallemant, S.E., Culotta, R., and Von Huene, R., 1989, Subduction of the Daiichi Kashima Seamount in the Japan Trench: *Tectonophysics*, v. 160, [https://doi.org/10.1016/0040-1951\(89\)90393-4](https://doi.org/10.1016/0040-1951(89)90393-4).
- Lanari, P., Vidal, O., de Andrade, V., Dubacq, B., Lewin, E., Grosch, E.G., and Schwartz, S., 2014, XMapTools: A MATLAB®-based program for electron microprobe X-ray image processing and geothermobarometry: *Computers & Geosciences*, v. 62, p. 227–240, <https://doi.org/10.1016/j.cageo.2013.08.010>.
- Leake, B.E., Woolley, A.R., Arps, C.E.S., Birch, W.D., Gilbert, M.C., Grice, J.D., Hawthorne, F.C., Kato, A., Kisch, H.J., Krivovichev, V.G., Linthout, K., Laird, J., Mandarino, J.A., Maresch, W.V., Nickel, E.H., Rock, N.M.S., Schumacher, J.C., Smith, D.C., Stephenson, N.C.N., Ungaretti, L., Whittaker, E.J.W., and Youzhi, G., 1997, Nomenclature of amphiboles: Report of the Subcommittee on Amphiboles of the International Mineralogical Association, Commission on New Minerals and Mineral Names: *Canadian Mineralogist*, v. 35, p. 219–246.
- Lipman, P.W., Norkar, W.R., Moore, J.G., Wilson, J.B., and Gutmacher, C.E., 1988, *The Giant Submarine Alike Debris Slide, Mauna Loa, Hawaii: The Journal of Geophysical Research*. *Solid Earth*, v. 93, p. 4279–4299, <https://doi.org/10.1029/JB093iB05p04279>.
- MacPherson, G.T., 1983, The Snow Mountain Volcanic Complex: An on-land seamount in the Franciscan Terrain, California: *The Journal of Geology*, v. 91, p. 73–92, <https://doi.org/10.1086/628745>.
- Magott, R., Fabbri, O., and Fournier, M., 2016, Subduction zone intermediate-depth seismicity: Insights from the structural analysis of Alpine high-pressure ophiolite-hosted pseudotachylite (Corsica, France): *Journal of Structural Geology*, v. 87, p. 95–114, <https://doi.org/10.1016/j.jsg.2016.04.002>.
- Martin, L.A.J., Hermann, J., Gauthiez-Putallaz, L., Whitney, D.L., Vitale-Brovarone, A., Fornash, K.F., and Evans, N.J., 2014, Lawsonite geochemistry and stability—Implication for trace element and water cycles in subduction zones: *Journal of Metamorphic Geology*, v. 32, p. 455–478, <https://doi.org/10.1111/jmg.12093>.
- Masson, F., Anvari, M., Djamour, Y., Walpersdorf, A., Tavakoli, F., Daignières, M., Nankali, H., and Van Gorp, S., 2007, Large-scale velocity field and strain tensor in Iran inferred from GPS measurements: New insight for the present-day deformation pattern within NE Iran: *Geophysical Journal International*, v. 170, p. 436–440, <https://doi.org/10.1111/j.1365-246X.2007.03477.x>.
- Massonne, H.-J., and Schreyer, W., 1987, Phengite geobarometry based on the limiting assemblage with K-feldspar, phlogopite, and quartz: *Contributions to Mineralogy and Petrology*, v. 96, p. 212–224, <https://doi.org/10.1007/BF00375235>.
- McMurtry, G.M., Watts, P., Fryer, G.J., Smith, J.R., and Imamura, F., 2004, Giant landslides, mega-tsunamis, and paleo-sea level in the Hawaiian Islands: *Marine Geology*, v. 203, p. 219–233, [https://doi.org/10.1016/S0025-3227\(03\)00306-2](https://doi.org/10.1016/S0025-3227(03)00306-2).
- Menant, A., Angiboust, S., Monié, P., Oncken, O., and Guignér, J.-M., 2018, Brittle deformation during Alpine basal accretion and the origin of seismicity nests above the subduction interface: *Earth and Planetary Science Letters*, v. 487, p. 84–93, <https://doi.org/10.1016/j.epsl.2018.01.029>.
- Mochizuki, K., Yamada, T., Shinohara, M., Yamanaka, Y., and Kanazawa, T., 2008, Weak interplate coupling by seamounts and repeating M–7 earthquakes: *Science*, v. 321, p. 1194–1197, <https://doi.org/10.1126/science.1160250>.
- Moghadam, H.S., Mosaddegh, H., and Santosh, M., 2013, Geochemistry and petrogenesis of the Late Cretaceous Haji-Abad ophiolite (Outer Zagros Ophiolite Belt, Iran): Implications for geodynamics of the Bitlis-Zagros suture zone: *Geological Journal*, v. 48, p. 579–602, <https://doi.org/10.1002/gj.2458>.
- Moghadam, H.S., Bröcker, M., Griffin, W.L., Li, X.H., Chen, R.-X., and O'Reilly, S.Y., 2017, Subduction, high-P metamorphism, and collision fingerprints in South Iran: Constraints from zircon U–Pb and mica Rb–Sr geochronology: *Geochemistry, Geophysics, Geosystems*, v. 18, p. 306–332, <https://doi.org/10.1002/2016GC006585>.

- Molinario, M., Leturmy, P., Guezou, J.C., Frizon de Lamotte, D., and Eshraghi, S.A., 2005a, The structure and kinematics of the southeastern Zagros fold-thrust belt, Iran: From thin-skinned to thick-skinned tectonics: *Tectonics*, v. 24, <https://doi.org/10.1029/2004TC001633>.
- Molinario, M., Zeyen, H., and Laurencin, X., 2005b, Lithospheric structure beneath the south-eastern Zagros Mountains, Iran: Recent slab break-off?: *Terra Nova*, v. 17, p. 1–6, <https://doi.org/10.1111/j.1365-3121.2004.00575.x>.
- Monié, P., and Agard, P., 2009, Coeval blueschist exhumation along thousands of kilometers: Implications for subduction channel processes: *Geochemistry, Geophysics, Geosystems*, v. 10, <https://doi.org/10.1029/2009GC002428>.
- Morgan, W.J., 1971, Convection plumes in the lower mantle: *Nature*, v. 230, p. 42–43, <https://doi.org/10.1038/230042a0>.
- Niu, Y., Collerson, K.D., Batiza, R., Wendt, J.I., and Regelous, M., 1999, Origin of enriched-type mid-ocean ridge basalt at ridges far from mantle plumes: The East Pacific Rise at 11°20'N: *Journal of Geophysical Research. Solid Earth*, v. 104, p. 7067–7087, <https://doi.org/10.1029/1998JB900037>.
- Omrani, J., Agard, P., Whitechurch, H., Benoit, M., Prouteau, G., and Jolivet, L., 2008, Arc-magmatism and subduction history beneath the Zagros Mountains, Iran: A new report of adakites and geodynamic consequences: *Lithos*, v. 106, p. 380–398, <https://doi.org/10.1016/j.lithos.2008.09.008>.
- Park, J.O., Tsuru, T., Kaneda, Y., Kono, Y., Kodaira, S., Takahashi, N., and Kinoshita, H., 1999, A subducting seamount beneath the Nankai accretionary prism off Shikoku, southwestern Japan: *Geophysical Research Letters*, v. 26, p. 931–934, <https://doi.org/10.1029/1999GL900134>.
- Ranero, C.R., and von Huene, R., 2000, Subduction erosion along the Middle America convergent margin: *Nature*, v. 404, p. 748–752, <https://doi.org/10.1038/35008046>.
- Ranero, C.R., Phipps Morgan, J., McIntosh, K., and Reichert, C., 2003, Bending-related faulting and mantle serpentinization at the Middle America trench: *Nature*, v. 425, p. 367–373, <https://doi.org/10.1038/nature01961>.
- Reagan, M.K., Ishizuka, O., Stern, R.J., Kelley, K.A., Ohara, Y., Blichert-Toft, J., Bloomer, S.H., Cash, J., Fryer, P., Hanan, B.B., Hickey-Vargas, R., Ishii, T., Kimura, J.-I., Peate, D.W., Rowe, M.C., and Woods, M., 2010, Fore-arc basalts and subduction initiation in the Izu-Bonin-Mariana system: *Geochemistry, Geophysics, Geosystems*, v. 11, <https://doi.org/10.1029/2009GC002871>.
- Rowe, C.D., Meneghini, F., and Moore, J.C., 2011, Textural record of the seismic cycle: strain-rate variation in an ancient subduction thrust: *Geological Society of London, Special Publications*, v. 359, p. 77–95, <https://doi.org/10.1144/SP359.5>.
- Ruh, J.B., Sallarès, V., Ranero, C.R., and Gerya, T.V., 2017, Crustal deformation dynamics and stress evolution during seamount subduction: High-resolution 3-D numerical modeling: *Journal of Geophysical Research. Solid Earth*, v. 122, p. 2069–2084, <https://doi.org/10.1002/2016JB013608>.
- Sabzehei, M., 1974, Les mélanges ophiolitiques de la région d'Esfaendagheh (Iran méridional)—Étude pétrologique et structurale - Interprétation dans le cadre iranien: *Université Scientifique et Médicale de Grenoble*, 306 p.
- Scambelluri, M., Pennacchioni, G., Gilio, M., Bestmann, M., Plümper, O., and Nestola, F., 2017, Fossil intermediate-depth earthquakes in subducting slabs linked to differential stress release: *Nature Geoscience*, v. 10, p. 960–966, <https://doi.org/10.1038/s41561-017-0010-7>.
- Schnur, S.R., and Gilbert, L.A., 2012, Detailed volcanostratigraphy of an accreted seamount: Implications for intraplate seamount formation: *Geochemistry, Geophysics, Geosystems*, v. 13, p. 1–13, <https://doi.org/10.1029/2012GC004301>.
- Schwartz, S., Guillot, S., Reynard, B., Lafay, R., Debret, B., Nicollet, C., Lanari, P., and Auzende, A.-L., 2013, Pressure-temperature estimates of the lizardite/antigorite transition in high pressure serpentinites: *Lithos*, v. 178, p. 197–210, <https://doi.org/10.1016/j.lithos.2012.11.023>.
- Searle, M., and Cox, J., 1999, Tectonic setting, origin, and obduction of the Oman ophiolite: *Geological Society of America Bulletin*, v. 111, p. 104–122, [https://doi.org/10.1130/0016-7606\(1999\)111<0104:TSAOAO>2.3.CO;2](https://doi.org/10.1130/0016-7606(1999)111<0104:TSAOAO>2.3.CO;2).
- Shervais, J.W., Schuman Zoglmann, M.M., and Hanan, B.B., 2005, The Stonyford volcanic complex: A forearc seamount in the Northern California Coast Ranges: *Journal of Petrology*, v. 46, p. 2091–2128, <https://doi.org/10.1093/petrology/egi048>.
- Singh, S.C., Hananto, N., Mukti, M., Robinson, D.P., Das, S., Chauhan, A., Carton, H., Gratacos, B., Midnet, S., Djajadihardja, Y., and Harjono, H., 2011, Aseismic zone and earthquake segmentation associated with a deep subducted seamount in Sumatra: *Nature Geoscience*, v. 4, p. 308–311, <https://doi.org/10.1038/ngeo1119>.
- Smith, W.H.F., and Sandwell, D.T., 1997, Global sea floor topography from satellite altimetry and ship depth soundings: *Science*, v. 277, p. 1956–1962, <https://doi.org/10.1126/science.277.5334.1956>.
- Spray, J.G., 1988, Generation and crystallization of an amphibole melt: An investigation using radial friction welding apparatus: *Contributions to Mineralogy and Petrology*, v. 99, p. 464–475, <https://doi.org/10.1007/BF00371937>.
- Staudigel, H., Koppers, A., Lavelle, J.W., Pitcher, T.J., and Shank, T.M., 2010, Box 1: Defining the word “seamount”: *Oceanography*, v. 23, no. 1, p. 20–21, <https://doi.org/10.5670/oceanog.2010.85>.
- Vannucchi, P., Fisher, D.M., Bier, S., and Gardner, T.W., 2006, From seamount accretion to tectonic erosion: Formation of Osa Mélange and the effects of Cocos Ridge subduction in southern Costa Rica: *Tectonics*, v. 25, <https://doi.org/10.1029/2005TC001855>.
- van Rijsingen, E., Lallemand, S., Peyret, M., Arcay, D., Heuret, A., Funicello, F., and Corbi, F., 2018, How subduction interface roughness influences the occurrence of large interplate earthquakes: *Geochemistry, Geophysics, Geosystems*, v. 19, p. 2342–2370, <https://doi.org/10.1029/2018GC007618>.
- Vernant, Ph., Nilforoushan, F., Hatzfeld, D., Abbassi, M.R., Vigny, C., Masson, F., Nankali, H., Martinod, J., Ashtiani, A., Bayer, R., Tavakoli, F., and Chéry, J., 2004, Present-day crustal deformation and plate kinematics in the Middle East constrained by GPS measurements in Iran and northern Oman: *Geophysical Journal International*, v. 157, p. 381–398, <https://doi.org/10.1111/j.1365-246X.2004.02222.x>.
- Vitale-Brovarone, A., Alard, O., Beyssac, O., Martin, L.A.J., and Picatto, M., 2014, Lawsonite metasomatism and trace element recycling in subduction zones: *Journal of Metamorphic Geology*, v. 32, p. 489–514, <https://doi.org/10.1111/jmg.12074>.
- Wang, K., and Bilek, S.L., 2011, Do subducting seamounts generate or stop large earthquakes?: *Geology*, v. 39, p. 819–822, <https://doi.org/10.1130/G31856.1>.
- Wang, K., and Bilek, S.L., 2014, Invited review paper: Fault creep caused by subduction of rough seafloor relief: *Tectonophysics*, v. 610, p. 1–24, <https://doi.org/10.1016/j.tecto.2013.11.024>.
- Watts, A.B., and ten Brink, U.S., 1989, Crustal structure, flexure, and subsidence history of the Hawaiian Islands: *Journal of Geophysical Research. Solid Earth*, v. 94, p. 10,473–10,500, <https://doi.org/10.1029/JB094iB08p10473>.
- Wenk, H.R., and Weiss, L.E., 1982, Al-rich calcic pyroxene in pseudotachylite: An indicator of high pressure and high temperature?: *Tectonophysics*, v. 84, p. 329–341, [https://doi.org/10.1016/0040-1951\(82\)90166-4](https://doi.org/10.1016/0040-1951(82)90166-4).
- Wessel, P., Sandwell, D.T., and Kim, S.-S., 2010, The Global Seamount Census: *Oceanography*, v. 23, no. 1, p. 24–33, <https://doi.org/10.5670/oceanog.2010.60>.
- Whitney, D.L., and Evans, B.W., 2010, Abbreviations for names of rock-forming minerals: *The American Mineralogist*, v. 95, p. 185–187, <https://doi.org/10.2138/am.2010.3371>.
- Wilson, J.T., 1965, Evidence from ocean islands suggesting movement in the Earth: *Philosophical Transactions of the Royal Society A: Mathematical, Physical and Engineering Sciences*, v. 258, p. 145–167, <https://doi.org/10.1098/rsta.1965.0029>.